Meteorol. Z. (Contrib. Atm. Sci.), Vol. **29**, No. 1, 19–39 (published online March 11, 2020)

Physically based correction of systematic errors of Rotating Shadowband Irradiometers

Anne Forstinger[1], Stefan Wilbert[1*], Anton Driesse[2], Natalie Hanrieder[1], Roman Affolter[3], Sharad Kumar[4], Neeraj Goswami[4], Norbert Geuder[5], Frank Vignola[6], Luis Zarzalejo[7] and Aron Habte[8]

[1]German Aerospace Center (DLR), Institute of Solar Research, Tabernas/Almería, Spain
[2]Photovoltaic Performance Labs, Freiburg Germany
[3]CSP Services, Almería, Spain
[4]NETRA, NTPC Ltd., E3 Ecotech II, Gautam Budh Nagar, India
[5]Hochschule für Technik, Stuttgart, Germany
[6]Univ. of Oregon Eugene, USA
[7]CIEMAT, Energy Department, Renewable Energy Division, Madrid, Spain
[8]NREL, Denver, USA

(Manuscript received May 2, 2019; in revised form August 11, 2019; accepted October 22, 2019)

Abstract

Accurate measurements of direct normal, diffuse horizontal and global horizontal irradiance (DNI, DHI and GHI) are needed for meteorological studies and are essential for the solar resource assessment at potential solar power plant sites. Often, these potential sites are remote and hence require robust sensors that require minimal maintenance that are not affected strongly by soiling. Therefore, Rotating Shadowband Irradiometers (RSI) are widely used for resource assessment. To achieve the required accuracy, corrections for the raw values of RSIs depending on systematic temperature, incidence angle and spectral errors must be used, and a thorough calibration of the sensor head must be applied. The existing correction functions are derived from comparisons of RSIs to thermopile radiometers at selected sites and therefore empirical. Their accuracy is considered to be site dependent. In this work a new correction and calibration method is presented that removes the systematic errors using a physical approach. It is based on information of the sensor properties as well as measurements of its directional response, and incorporates the atmospheric conditions at the measurement site. In this case, no empiric relations obtained from a specific site are required. The method requires estimates of the current DHI and GHI spectra during each measurement of the RSI. Based on these spectra, a spectral correction, which includes a spectrum dependent temperature correction, can be made without employing empirical relationships. The new physical calibration and correction method is tested at three sites and reaches similar results compared to the empirical functions. This is already achieved with rudimentary estimations of the GHI and DHI spectra and we expect that these estimations can be improved in the future. The results indicate that the physical approach reduces the problematic location dependence of the current calibration and correction methods. The physical correction and calibration method show promise for a further improvement of the RSI accuracy.

Keywords: Rotating Shadowband radiometer, radiometer calibration, pyranometer, spectral error

1 Introduction

Accurate measurements of direct normal and global horizontal irradiance (DNI and GHI) are required for many applications ranging from weather forecasting over climate studies and energy meteorology. For big solar power plant projects, it is important to know the available solar resource at the location as accurately as possible. For the qualification of a power plant site irradiance measurements over one year or more taken close (<2 km) to the envisioned plant site are required (Sengupta et al., 2017). The most accurate measurement stations for continuous measurements under well-maintained conditions consist of three thermopile radiometers, that separately measure the direct normal irradiance (DNI), diffuse horizontal irradiance (DHI) and global horizontal irradiance (GHI) (Vuilleumier et al., 2014). To reduce the effect of soiling, these sensors have to be cleaned daily for the best performance (Sengupta et al., 2017). While the measurement accuracy achieved by these measurement stations under well-maintained conditions is high, the cleaning and acquisition costs are high as well. The cleaning costs are especially important when the desired location is remote and impedes daily cleaning thus finally leading to reduced accuracy.

Rotating Shadowband Irradiometers (RSIs) (Fig. 1) determine all three irradiance components with one sensor that is less affected by soiling as documented by Maxwell et al. (1999), Geuder and Quaschning

*Corresponding author: Stefan Wilbert, Institute of Solar Research, Paseo de Almería, 73-2, 04001 Almería, Spain, e-mail: stefan.wilbert@dlr.de

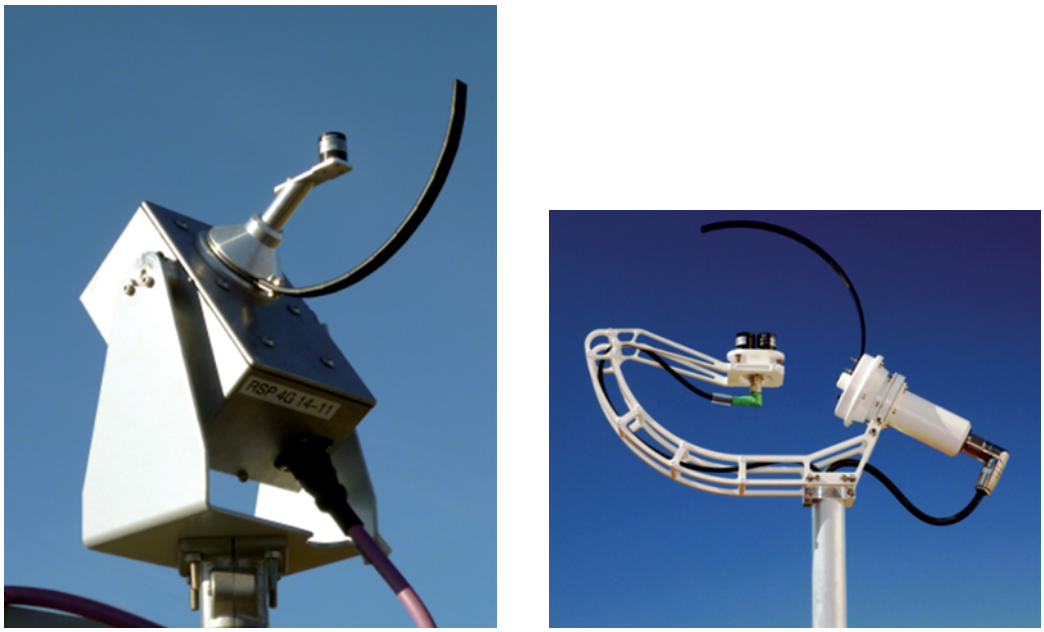

Figure 1: Left: Reichert Rotating shadowband irradiometer in rest position. Right: CSPS Twin RSI during the rotation.

(2006) and Pape et al. (2009). Most RSIs use silicon photodiode pyranometers positioned horizontally in the center of a circular rotatable shadowband. The pyranometer measures GHI while the shadowband is below the sensor surface. The shadowband rotates around the pyranometer once or twice per minute with a duration of the complete rotation of roughly 1.5 seconds. During the rotation the signal is measured with high sampling rate in order to identify the irradiances when the shadow falls on the pyranometer and when the shadowband covers the bright region close to the sun. Using these irradiances, the DHI can be determined and finally the DNI can be calculated with the solar elevation angle. To obtain 1-minute averages, the GHI is sampled each second and a linear interpolation of the two or three DHI measurements within the minute is used to obtain estimations of the DHI and DNI in 1-sec resolution. These 1-second time series are then averaged to 1-minute resolution, RSIs are not as accurate under well-maintained conditions with daily cleaning, but can reach higher accuracies than thermopile sensors if no daily maintenance is provided (Wilbert et al., 2015). Studies of the RSI accuracy can be found in Wilbert et al. (2016); Vuilleumier et al. (2017). Furthermore, RSIs can be programmed to measure circumsolar radiation which is of interest for concentrating solar power plants and atmospheric studies (Wilbert et al., 2018).

The silicon pyranometers have a non-uniform spectral response over the solar spectrum (0.28–4 µm) which depends on the temperature Vignola et al. (2016), King-Smith et al. (1989) and their optics fail to mimic an ideal cosine response at large solar zenith angles. Therefore, RSI measurements are affected by systematic errors that depend on the incoming solar spectrum, the sensor temperature and the incidence angle of the incoming radiation. The spectral irradiance error is the error introduced by the change in the spectral distribution of the incident solar radiation over the day and the difference between the spectral response of the photodiode-based radiometer used by the RSI with respect to a radiometer with uniform spectral response from 0.28 to 4 µm. In order to remove these systematic errors, specific correction functions can be applied. Current correction methods have been developed using empirical relationships by comparing the RSI measurements to thermopile measurements. These corrections reduce the temperature, incidence angle and spectral error of the RSI measurement. However, such correction functions are more accurate at the site at which they were developed than at a site with noticeably different climate, as e.g. the prevailing solar spectra and the spectral errors deviate between sites (Geuder et al., 2016). Furthermore, the temperature corrections applied so far are not linked to the spectral corrections. However, the spectral responsivity of the pyranometer changes with the temperature which links the spectral and the temperature errors.

The new correction and calibration method, which is presented in this paper, attempts to correct the measurement errors using a physical method. It is based on information of the sensor properties and the atmospheric conditions at the measurement site. This way, no site-specific empirical relations are required. The method requires estimates of the current DHI and GHI spectra during each measurement of the sensor. Based on these spectra, a spectral correction, which includes a spectrum dependent temperature correction, can be made without employing empirical relationships. A prerequisite for this method is accurate knowledge of the silicon pyranometer's characteristics, which can be obtained through a combination of indoor and outdoor methods as done in the PVSENSOR study (Driesse et al., 2015).

Sections 1.1 and 1.2 give a general overview of existing RSI correction functions as well as RSI calibration. In Section 2 the development of the new correction and corresponding calibration method is described. The evaluation of the method at two locations as well as possible improvements of the new correction method are discussed in Section 3 before a conclusion and summary.

1.1 State of the art of correction functions for RSIs

The systematic cosine, temperature and spectral errors of RSIs can be reduced using correction functions. Several different correction functions were developed to account for these systematic errors, for example the set of correction functions by King and Myers (1997); Augustyn et al. (2004); Vignola (2006) or by Geuder et al. (2008). The correction functions by King and Myers (1997); Augustyn et al. (2004); Vignola (2006) are in the following referred to as *Vig*. They are based on a GHI correction that is described as

$$GHI_{Vig} = GHI_{\text{raw}} \cdot \frac{F_\alpha}{F_A \cdot F_B \cdot F_C} \tag{1.1}$$

with the temperature correction factor F_α (dependent on the sensor's temperature), the spectral response parameter F_A (dependent on the absolute air mass), and the cosine response parameter F_B and cat ear parameter F_C (both dependent on the solar zenith angle). The cosine response and cat ear parameter both aim to correct the systematic errors associated with the sensor geometry and the change of the diffusor disk's transmittance with the incidence angle. The diffusor disk is a cylinder whose upper surface and part of the lateral surfaces are exposed to the solar radiation. The transmittance of the upper surface decreases with increasing incidence angle. This is partly compensated by the lateral area of the diffusor which contributes more to the sensor signal for higher incidence angles. These parameters are calculated with functions that are linear or polynomial fits through the deviations between co-located RSI and thermopile measurements. After the GHI correction, the DHI is multiplied with a correction factor derived as a polynomial of the corrected GHI, representing the spectral correction. Finally, DNI is calculated from the corrected GHI, the corrected DHI and the solar elevation angle. The exact functions are documented in e.g. King and Myers (1997); Augustyn et al. (2004); Vignola (2006); Jessen et al. (2017). Since the functions are fit functions through measurements at a specific site, the functions depend on the climate conditions of that site and cannot be easily adjusted to other conditions such as e.g. high aerosol load.

(Geuder et al., 2008) also developed RSI correction functions, in the following referred to as *Geu*. First a temperature correction is applied on GHI and DHI data. The application of the temperature correction differs from the temperature correction of *Vig* in terms of a slightly different slope that was measured at the Plataforma Solar de Almería (PSA) in southern Spain using the sun as a light source. The DHI is corrected for the spectral error with a spectral correction parameter which has also been obtained as a fit function through empirical measurements. The spectral correction parameter is calculated from the broadband temperature corrected GHI, DHI and DNI to account for DHI underestimations under deep blue skies. The GHI is then corrected for incidence angle effects. At last, the DHI and DNI are corrected with cubic and linear functions that depend on the irradiances.

Further correction functions such as Geuder et al. (2011); Geuder et al. (2016); Batlles et al. (1995) are also available and summarized in Wilbert et al. (2015). The method of Vignola et al. (2017) is of particular interest for the approach presented here. In a first step the temperature correction is performed for DHI component and on the DNI component, modeled from the measured DHI and GHI. Then a spectral correction is applied for modeled DNI and DHI. The spectral correction for DHI is different for clear sky and cloudy sky cases which is the main difference to other correction functions. The spectral adjustment factors are based on the spectral response data of the pyranometer and spectra created for the expected atmospheric conditions at the site using a clear sky model. The conditions are assumed to be constant throughout the year. For cloudy conditions the DHI correction also includes an additional empirical correction term. For skies with some or total cloud cover, the DHI correction factor is adjusted depending on the level of DHI and DNI. This comes from the assumption that under totally cloudy skies, the DHI responsivity will be close to the responsivity for the direct horizontal irradiance spectrum. The responsivity is obtained as a mix of clear sky responsivity and total cloud cover responsivity. An incidence angle correction finalizes the DNI correction and then GHI is calculated from DNI and DHI. The incidence angle correction is derived from the remaining error after the temperature correction and spectral correction of DNI. Because this method uses the spectral irradiance data adapted to the site for clear skies, it has the potential to reduce the site dependence of the measurement uncertainty and the calibration.

In this paper, the newly developed correction functions are not developed based on empirical measurements but solely based on the correction of the physical measurement principal of the RSI (see Section 2).

1.2 State of the art of RSI calibration

For the calibration of RSIs, different procedures are used by the manufactures or providers. For some calibration methods, the RSI is deployed next to a reference station that consists of thermopile sensors for the measurement of the GHI, DHI and DNI. The calibration duration is between one and two months for the methods *Vig* and *Geu* as described in Jessen et al. (2016). For a *Vig* calibration, the GHI RSI measurement is corrected first.

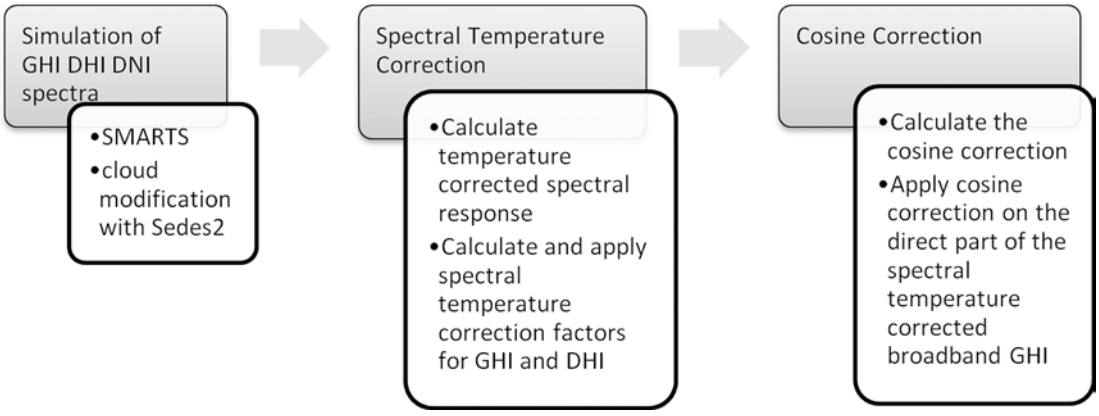

Figure 2: Basic concept of the physical correction method.

The GHI calibration factor is then obtained by minimizing the root mean square deviation (RMSD) between the corrected and the reference GHI. After applying the GHI calibration factor to the GHI, the DHI is corrected and a DHI calibration factor is obtained by minimizing the RMSD between the corrected and the reference DHI. Finally, a DNI calibration factor is determined by minimizing the RSMD between the calculated DNI from the RSI and the reference DNI.

For the calibration with *Geu* two calibration factors are determined. At first, the DHI is corrected and the DHI calibration factor is determined from the minimization of the RMSD between the corrected and the reference DHI. The GHI calibration factor is then obtained by minimizing the RMSD of the calculated DNI from the corrected GHI and the corrected DHI, multiplied with its calibration factor, and the reference DNI. Other calibration methods only compare the RSI's GHI to a reference GHI under specific irradiance conditions and solar positions (Kern, 2010).

2 Development of the physical correction and calibration method

In this section, the physical correction process is described. First, the basic concept as well as the new spectral temperature and cosine correction are presented. Then the creation of the spectra and the application of the correction method are explained.

2.1 Basic concept of the physical correction

The basic concept behind the physical correction function is illustrated in Fig. 2. First, the current DNI, GHI and DHI spectra are simulated with the clear sky radiative transfer model SMARTS 2.9.5 (Gueymard, 2005) and modified for the presence of clouds using the enhanced Sedes2 model (Nann and Riordan, 1990; Nann and Riordan, 1991; Jessen et al., 2018) with the best available input parameters. The resulting spectra are then used to calculate the temperature corrected spectral response for the current temperature. With that spectral response and the current spectrum, a combined spectral and temperature correction factor can be calculated for GHI and DHI, respectively. Then, a new cosine correction based on lab measurements (Driesse, 2018) is calculated and applied to the direct part of the spectral temperature corrected broadband GHI. With these corrected GHI and DHI values, the associated DNI is calculated. The physical correction is applied to 1-minute averages of the RSI measurements.

In the following, the determination of the specific spectral response and following spectral temperature correction as well as the cosine correction are described in detail. A flowchart of the calibration method is provided in the appendix.

2.1.1 Simulation of the GHI, DHI and DNI spectra

The simulation of the spectrum is carried out with a combination of SMARTS 2.9.5 and an enhanced version of Sedes2. The required input for these calculations is obtained as explained in the following.

The ambient temperature, relative humidity and pressure are measured at a meteorological station. The current true sun height and the apparent solar height angle with refraction are calculated along equations by Michalsky (1988). The pressure corrected, uncorrected and altitude corrected air mass are calculated as done by Kasten and Young (1989)). The current CO_2 concentration is estimated with a simple model including the seasonal variation of CO_2 provided by Olsen and Randerson (2004) along the method described by Wilbert (2014), p.56. The, possibly seasonally dependent, albedo has to be selected by the user using the options implemented in SMARTS 2.9.5 (Gueymard, 2005).

Some of the input parameters are obtained from different sources depending on whether or not the corrections are performed during the calibration of the RSI or during its application in the field. During the calibration some input parameters are obtained by reference sensors such as an Aeronet sun photometer, which are typically not available at RSI stations.

The aerosol optical depth (AOD, τ_λ) is of particular interest for the determination of the spectra. During the calibration, aerosol data from a co-located Aeronet station can be used to calculate the AOD with a modified Angström spectral AOD dependency using exponents α_i and turbidity coefficients β_i along

$$\tau_\lambda = \beta_i \left(\frac{\lambda}{1000\,\mathrm{nm}} \right)^{-\alpha_i} \tag{2.1}$$

where α_1 is used for wavelengths below 500 nm and α_2 above this wavelength. β_i is β above 500 nm and $2^{\alpha_2-\alpha_1}\beta$ below 500 nm (Gueymard, 2001). The broadband single scattering albedo and asymmetry factor are calculated by weighing their spectral components with a GHI spectrum under ASTM G173 atmospheric conditions (ASTM, 2012) at a rough estimate of the apparent air mass (Wilbert, 2014). The Aeronet station also provides the ozone concentration and the precipitable water vapor (WV) during the RSI calibration. While WV is measured using the 935 nm, the ozone is obtained using London et al. (1976), Komhyr et al. (1989) and Holben et al. (1998). All these parameters have to be estimated for the application of the correction when the RSI is deployed for a resource assessment campaign as described in Section 2.3.

Using these values, the clear sky spectra for DNI, DHI and GHI are estimated with a SMARTS 2.9.5 simulation. The resulting spectra for GHI and DNI are then corrected with the enhanced Sedes2 model. The model derives the clearness index based on the GHI broadband measurement and the extraterrestrial irradiance. The clearness index is then used to calculate a cloud cover modifier for the GHI spectra. This modifier is an empirical relationship developed with GTI (global tilted irradiance) data from Stuttgart, Germany (Nann and Riordan, 1991). Myers (2012) altered the original algorithm for the processing of hourly broadband global, diffuse and direct irradiance to their corresponding spectra. The algorithm used here is altered in such a way that the spectra of the GHI and DNI are further modified for the cloud effects (Jessen et al., 2018). The model assumes that clouds act as grey filters on the DNI spectra. The corresponding transmittance is derived from the clear sky DNI from SMARTS and the measured DNI. Another enhancement of the applied model compared to the original Sedes2 model is related to over-irradiance. If the measured GHI (GHI_{meas}) is above the clear sky GHI from SMARTS (GHI_{clearsky}) clouds are assumed to scatter a fraction of the clear sky direct irradiance (DNI_{clearsky}) onto the surface. The contribution of this scattered DNI is determined such, that the sum of clear sky GHI and scattered DNI result in the measured GHI. The spectral all sky GHI is calculated as

$$GHI_{s,\mathrm{allsky}}(\lambda) = GHI_{s,\mathrm{clearsky}}(\lambda) + DNI_{s,\mathrm{clearsky}}(\lambda) \cdot \frac{GHI_{\mathrm{meas}} - GHI_{\mathrm{clearsky}}}{DNI_{\mathrm{clearsky}}} \tag{2.2}$$

using the spectral clear sky GHI ($GHI_{s,\mathrm{clearsky}}$) and DNI ($DNI_{s,\mathrm{clearsky}}$).

For this cloud modification, the most accurate available measurements of the broadband GHI and DNI are used to determine the right cloud modifier. During the calibration the required GHI and DNI come from the thermopile radiometers at the reference station, which is located nearby the RSI under calibration. For the application of the method at a remote site without a reference station which is resolved by taking the best available preliminary GHI and DNI from the RSI are used as further explained in Section 2.3. Finally, the cloud corrected spectra for GHI and DNI are then used to calculate the DHI spectra.

2.1.2 Description of the combined spectral and temperature correction

The Si pyranometer of the RSI has a temperature dependent spectral response. The temperature effect is especially dominant in the range of 1000 to 1200 nm, where the indirect band-gap of silicon is located (Rajkanan et al., 1979). Therefore, the responsivity R_{bb} of the pyranometer to broadband irradiance, depends on the spectral response at temperature T, $\mathrm{R}_s(\lambda, T)$, the spectral irradiance $\mathrm{I}_s(\lambda)$ and the temperature T:

$$R_{bb} = \frac{\int d\lambda R_s(\lambda, T) \cdot I_s(\lambda)}{\int d\lambda I_s(\lambda)}. \tag{2.3}$$

Here, the spectral response $R_s(\lambda)$ is normalized to 1 at its maximum. The short circuit current of the silicon pyranometer is proportional to the product of the responsivity R_{bb} and the incoming broadband irradiance.

In order to incorporate the temperature dependence of the spectral response into the spectral correction, the wavelength per temperature shift of the quantum efficiency described by Hishikawa et al. (2018) for silicon based photovoltaic devices is used. The quantum efficiency (QE) can be calculated from the spectral response using a constant C_{QE} as

$$QE(\lambda) \cong R_s(\lambda) \cdot \frac{C_{QE}}{\lambda}. \tag{2.4}$$

For Hishikawa et al.'s approach the wavelength $\boldsymbol{\lambda}_{\mathrm{max}}$ at which the quantum efficiency is maximum, is determined. To calculate the quantum efficiency at a desired temperature $\boldsymbol{T_2}$, the quantum efficiency at temperature $\boldsymbol{T_1}$ is shifted by $\boldsymbol{-0.45\Delta T \frac{\mathrm{nm}}{\mathrm{K}}}$ in wavelength above $\boldsymbol{\lambda}_{\mathrm{max}}$. $\boldsymbol{\Delta T}$ is the temperature difference between $\boldsymbol{T_1}$ and $\boldsymbol{T_2}$. Below $\boldsymbol{\lambda}_{\mathrm{max}}$ the quantum efficiency at $\boldsymbol{T_2}$ equals the quantum efficiency at $\boldsymbol{T_1}$ (Hishikawa et al., 2018):

$$QE(\lambda, T = T_2) = \begin{cases} QE(\lambda - 0.45\frac{\mathrm{nm}}{\mathrm{K}} \cdot \Delta T, T = T_1) & \lambda > \lambda_{\mathrm{max}} \\ QE(\lambda, T = T_1) & \lambda \leq \lambda_{\mathrm{max}} \end{cases}. \tag{2.5}$$

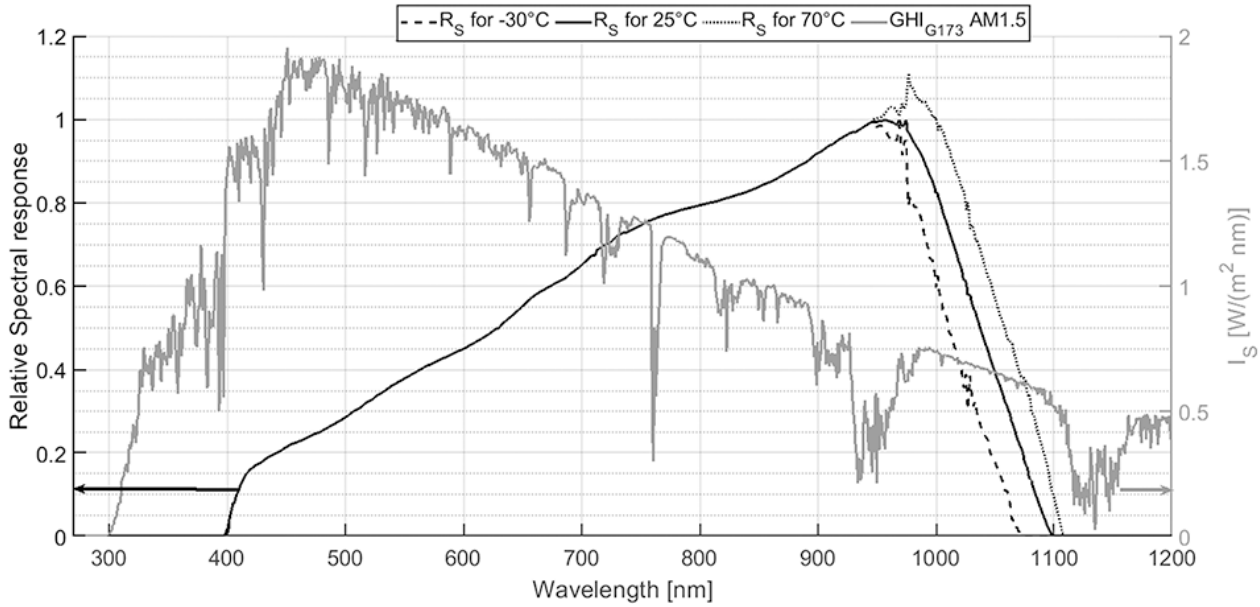

Figure 3: Calculated spectral response (R_S) of the LI-200 at −30 °C, 25 °C and 70 °C pertinent to the left axis and the spectral irradiance (I_S) of the GHI under G173 conditions pertinent to the right axis.

Finally, the quantum efficiency at T_2 is converted back to the spectral response at T_2 with Eq. (2.4). The resulting spectral response is not normalized anymore. Values above one are reached at higher temperatures which shows that the pyranometer's responsivity to broadband radiation is higher at higher temperatures. The manufacturer of the LI-200 silicon pyranometer that is used in this study provides a generic spectral response (Licor, 2004). It is not clear from the provided information by Licor (2004) at which temperature this spectral response is measured, but we assume the temperature to be 25°C because this is the standard temperature for laboratory conditions. Using the above described method with the generic spectral response, the spectral response at different temperatures can be calculated. Fig 3 shows the obtained spectral response curves for different temperatures for −30 °C, 25 °C and 70 °C as calculated with the model and the GHI spectrum under G173 conditions for comparison.

After deriving the spectral response at the current sensor temperature, the broadband responsivities can be calculated using Eq. (2.3). Broadband refers to the range from 280 nm to 4000 nm in this work. The integrals are calculated numerically using trapezoid integration as defined in ASTM (2016). With the obtained responsivities, the spectral temperature correction factor $F_{\alpha F,I}$ for the irradiance I can be defined

$$F_{\alpha F,I} = \frac{\int d\lambda R_s(\lambda, T_{\text{ref}}) \cdot I_{s,\text{G173}}(\lambda)}{\int d\lambda R_s(\lambda, T_{\text{curr}}) \cdot I_{s,\text{curr}}(\lambda)} \cdot \frac{\int d\lambda I_{s,\text{curr}}(\lambda)}{\int d\lambda I_{s,\text{G173}}} = \frac{R_{bb}^{\text{ref}}}{R_{bb}^{\text{curr}}} \tag{2.6}$$

where T_{ref} is the reference temperature, here 25 °C, T_{curr} the current temperature, $I_{s,\text{G173}}(\lambda)$ the reference spectrum of the DHI or GHI under G173 conditions and $I_{s,\text{curr}}(\lambda)$ the current spectrum of the DHI or GHI. For a given time stamp, $F_{\alpha F,\text{GHI}}$ and $F_{\alpha F,\text{DHI}}$ are calculated for DHI and GHI, respectively. For GHI the uncorrected GHI GHI_{raw} is used to obtain the spectral and temperature corrected GHI as:

$$GHI_{\text{spectemp}} = F_{\alpha F,\text{GHI}} \cdot GHI_{\text{raw}} \tag{2.7}$$

For the conversion of the uncorrected DHI (DHI_{raw}) to the spectral and temperature corrected DHI (DHI_{spectemp}), another factor is included in order to obtain DHI calibration factors close to one. Each LI-200 sensor is calibrated beforehand by LI-COR Biosciences by comparing the GHI from the silicon pyranometer to a thermopile pyranometer (Licor, 2004, p.7). The obtained calibration factor is applied to the measurements of the GHI, DHI and DNI by default in the RSI's data logger (Jessen et al., 2017). However, the calibration factor from LI-COR is derived for GHI and is inappropriate for DHI because of the different spectra of GHI and DHI. Therefore, the later derived DHI calibration factors would be greater than 1 if no further additional factor is included. Calibration factors close to 1.0 have the advantage that the individual sensor's deviation from the common expected sensitivity is obvious. Therefore, we apply such a convenient additional factor to DHI. We calculate this factor using Eq. (2.6) with the LI-200 spectral response (Licor, 2004) and the GHI spectrum under G173 conditions as reference spectrum and DHI spectrum under G173 conditions as current spectrum. This factor of 1.279 is

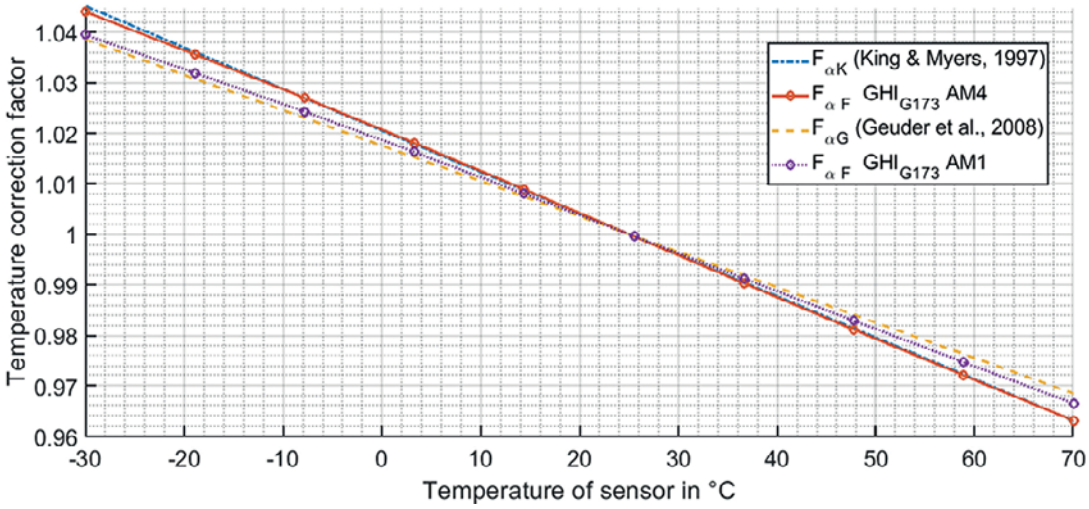

Figure 4: Spectral temperature correction factors $F_{\alpha F}$ for the GHI spectrum under G173 atmospheric conditions with different air masses in comparison with currently used broadband temperature correction factors $F_{\alpha G}$ as obtained by Geuder et al. (2008) and $F_{\alpha K}$ as obtained by King and Myers (1997).

applied to the DHI measurement of the RSI additionally to the LI-COR constant, before the measurements are further corrected. The factor reflects the fact that the LI-COR pyranometer's responsivity for GHI is 1.279 times higher than for DHI under G173 conditions at 25 °C.

$$DHI_{\text{spectemp}} = 1.279 F_{\alpha F,\text{DHI}} \cdot GHI_{\text{raw}} \qquad (2.8)$$

The spectral temperature correction factors $F_{\alpha F,\text{GHI}}$ and $F_{\alpha F,\text{DHI}}$ have the advantage that they refer to standard conditions (spectra for G173 conditions at air mass 1.5 and $T_{\text{ref}} = 25\,°\text{C}$), which is useful for the later definition of calibration factors (see Section 2.2 below). It also combines the temperature and spectral correction into one correction factor. These functional dependences (Eq. (2.3) to (2.8)) of the responsivity of the sensor and the spectral and temperature corrected GHI and DHI are applied during the calibration and the correction of the sensor.

Comparison of the obtained temperature correction to pre-existing temperature corrections

King and Myers (1997) and Geuder et al. (2008) calculated a broadband temperature correction $F_{\alpha K}$ and $F_{\alpha G}$ that can now be compared with $F_{\alpha F}$

$$F_{\alpha K} = 1 - \alpha_K (T_{\text{RSI}} - T_{\text{ref}}) \qquad (2.9)$$

with $\alpha_K = -0.00082/\text{K}$ King and Myers (1997). Geuder et al. (2008) uses the same linear relation, but with $\alpha_K = -0.0007/\text{K}$. Fig. 4 shows the temperature correction factors as a function of the sensor temperature. To compare the new correction to these functions from literature, $F_{\alpha F}$ is calculated for a fixed GHI spectrum under G173 atmospheric conditions at a specific air mass and different temperatures. The slope α_F corresponding to Eq. (2.7) is then obtained via linear regression. α_F is $-0.00083/\text{K}$ for an air mass of 4 and $-0.00079/\text{K}$ for an air mass of 1 (Vignola et al., 2019).

The measurements carried out by Geuder et al. (2008) to obtain $F_{\alpha G}$ were conducted at the Plataforma Solar de Almeria, in southern Spain. For the experiment, the used LI-200 was cooled down to 0 °C and then mounted outside close to solar noon. As the sensor heated up to 40 °C, the sensor signal was measured as well as the temperature inside the sensor. To account for changes of the irradiance during the measurement campaign, a reference photodiode at a constant temperature measured the irradiance near by the unit under test (Geuder et al., 2008). The facts that the experiment was conducted around solar noon and with a high maximum temperature lead to an air mass close to one. As Fig. 4 shows, the newly obtained $F_{\alpha F}$ for air mass 1 ($F_{\alpha F}\ GHI^{\text{G173}}\ AM1$) fits the curve obtained by Geuder et al. (2008), $F_{\alpha G}$, quite well. This was also expected as the average conditions at PSA are close to G173 conditions (Jessen et al., 2018).

It could not be determined exactly under which specific conditions the experiment from King and Myers (1997) was conducted. The publication only states that the temperature correction was determined with a routinely used standard for photovoltaic cells (King and Myers, 1997). The resulting $F_{\alpha F}$ from King and Myers (1997) can be reproduced using $AM4$.

2.1.3 Description of the cosine correction

In previous works, the cosine correction functions (also called incidence angle modifiers, IAM) were determined outdoors, and were thus subject to changes in spectrum, temperature and diffuse fraction over the course of the measurements (King et al., 1997; Geuder et al., 2008). For the present study we used directional response measurements of the LI-200 carried out in the laboratory by PV Performance Labs Germany in the

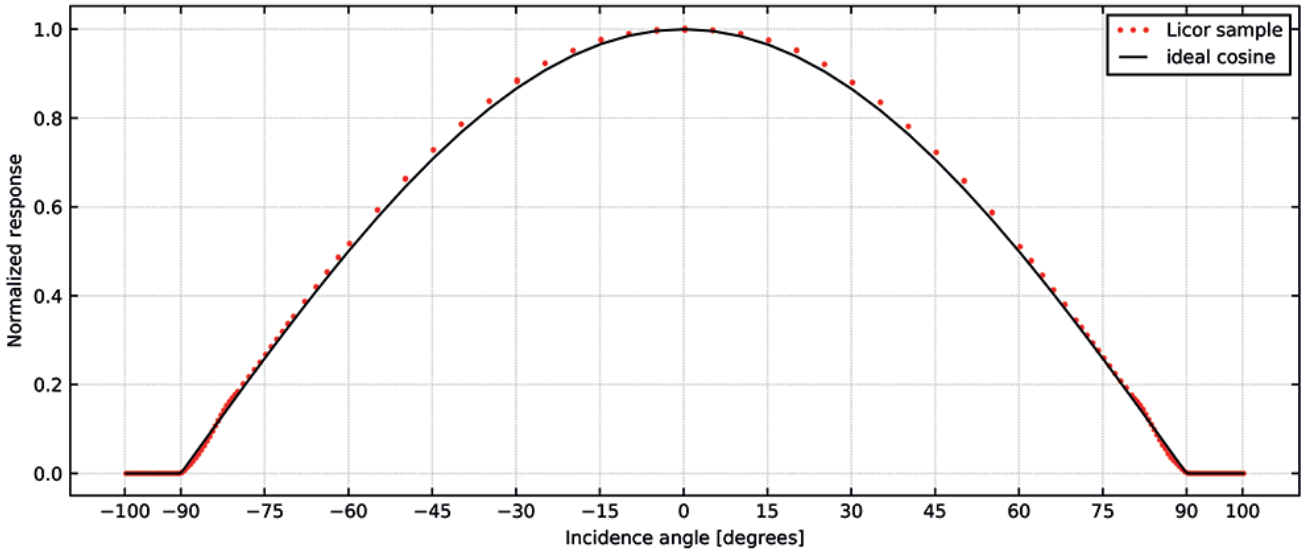

Figure 5: Normalized response of an LI-COR sensor and the ideal cosine plotted against the incidence angle of the light source.

context of the PVSENSOR project (Driesse et al., 2015; Driesse, 2018). In essence, the sensors were mounted on a computer-controlled rotating platform, illuminated by a stable distant light source, and shaded from any stray light or reflections. The platform was then rotated through a predetermined sequence of angles over the range −100° to +100° (10° below the sensor surface on each side) with increments as small as 0.5°, and a positioning accuracy <0.1°. The output signal of the sensor was measured at each position and normalized afterwards to the signal level at 0° angle of incidence. The resulting response of one LI-COR sample dependent on the incidence angle of the incoming light is shown in Fig. 5 as well as the ideal cosine for comparison. This absolute directional response was then divided by the ideal cosine response to produce the new cosine correction function $\boldsymbol{F}_{\cos}$. The angular resolution of the measurements is high enough that a simple interpolation can be used, but for this work a polynomial spline fit to the data was preferred. The correction factor $\boldsymbol{F}_{\cos}$ corrects the signal to the ideal cosine of the current incidence angle. Because of the measurement technique, the correction factor can be applied as a stand-alone function to the DNI as opposed to the currently published cosine and cat ear correction factors that depend on the air mass correction function and are applied to the GHI (see Section 1.1) (King and Myers, 1997; Vignola, 2006; Geuder et al., 2008). For incidence angles between 0° and 80°, the correction factor varies between 1 and 0.96 and above 80° between 0.94 and 1.4.

This cosine correction factor is applied to the direct component of the spectrally and temperature corrected GHI along:

$$GHI_{\text{spectempcos}} = (GHI_{\text{spectemp}} - DHI_{\text{spectemp}}) \cdot F_{\cos}(SZA) + DHI_{\text{spectemp}} \quad (2.10)$$

The calibration method and application of the corrections and calibration factors in the field are described in the following two Sections 2.2 and 2.3.

2.2 Calibration procedure

To obtain the final RSI measurements, the calibration factors are applied. Two calibration factors g and d are defined for GHI and DHI respectively for each sensor, since the spectral response might vary between different sensors. The fully corrected GHI and DHI measurements of the RSI are calculated as follows with the GHI calibration factor g and the DHI calibration factor d:

$$GHI_{\text{final}} = g \cdot GHI_{\text{spectempcos}} \quad (2.11)$$

$$DHI_{\text{final}} = d \cdot DHI_{\text{spectempcos}} \quad (2.12)$$

From the final resulting GHI_{final} and DHI_{final}, the corresponding DNI_{final} can be calculated.

Because of the simulation of the spectra during the physical correction, additional reference sensors are used for the calibration of the RSIs. First of all, just like for the calibration using *Vig* or *Geu* functions, a reference station with a pyrheliometer and two thermopile pyranometers for GHI, DHI is used. Also, the pressure, ambient temperature and relative humidity are measured. Additionally, an Aeronet station is used that provides the ozone concentration, precipitable water vaper and measurements for the calculation of the Angström turbidity factor and exponents, single scattering albedo and asymmetry factor. In the best case, the RSI itself needs to have an internal temperature sensor to measure the temperature of the photodiode sensor. If this is not the case, the RSI pyranometer temperature can be estimated based on the air temperature (Wilbert et al., 2015). During the calibration measurement period of at least one and a half months, the weather conditions

should be cloudy as well as clear periods so that the sensor is calibrated for these conditions.

After the measurements are conducted, the raw data are quality controlled and filtered using methodologies from Geuder et al. (2015) to calibrate only reliable measurement data. The RSI measurements are corrected using the physical correction method. In summary, the spectra of the GHI and DHI are simulated for each time stamp as described above. Using the temperature of the silicon pyranometer, the spectral response is calculated for each time stamp as well. Then, the spectral and temperature correction factors $F_{\alpha F}$ for GHI and DHI are calculated for each time stamp using the specific spectrum and spectral response. Also, each individual GHI_{spectemp} is cosine corrected.

To obtain the calibration factor g for the GHI, g is varied and the RMSD of the corresponding GHI_{final} and the reference GHI is derived. The g minimizing the RMSD is selected as the calibration result using a minimum search algorithm. In order to calculate the calibration factor d for the DHI, d is varied such that the RMSD of DNI_{final} and the reference DNI is minimized. In contrast to the 10 min temporal averages used in Jessen et al (2016), temporal averages of 1 min are used for the calibration in order to allow for a more accurate distinction between clouds and aerosols. The calibration factors g and d are determined for each individual sensor during the calibration of the sensor. Using the correction method explained in the following, these calibration factors are used to correct the measurements of the individual sensor when it is deployed in a measurement campaign. This means that the calibration does not have to be repeated at a measurement site in a different climate.

2.3 Estimation of the spectra for the application of the correction method

As mentioned above in Section 2.1.1 some of the input parameters used for the estimation of the spectra during the calibration are not measured for most RSI measurement campaigns. These parameters are those measured by the Aeronet station and the reference irradiances. Especially the aerosol parameters (β_1, β_2, α_1, α_2, single scattering albedo and asymmetry factor) and the precipitable water vapor are of importance and complex to determine. The process will be described in the example that follows for an already measured time range of raw data from the RSI during a measurement campaign.

First, just like during the calibration, the solar position, different air masses and average temperature are calculated. Additionally, the precipitable water vapor is estimated from temperature, relative humidity and pressure along the formula provided by Garrison and Adler (1990) which is also implemented in SMARTS. Aerosol parameters, such as the Angström exponents α_1, α_2, the single scattering albedo and the asymmetry factor are set to temporally constant values. They are derived by evaluating a year of Aeronet data from the station that is expected as most representative for the site of interest and defined once beforehand. The temporal average of the spectral single scattering albedo and the asymmetry factors are calculated from the Aeronet data sets. These temporal averages are then spectrally weighted with the GHI spectrum under G173 air mass 1.5 spectral conditions to obtain the broadband single scattering albedo and asymmetry factor required for SMARTS. It is possible to provide seasonal values for these four parameters if more detailed information is available. These four parameters are kept to the default initial values throughout the correction process. In this work, a year of ozone concentrations from the selected Aeronet station is provided to the correction method to account for the large seasonal dependence of the ozone concentration over the course of one year. This can be improved in the future. Instead of Aeronet data, also other data sources could be used for aerosol and ozone information, i.e. satellite derived information.

In the next step, the current AOD at 550 nm has to be estimated in order to simulate the spectrum appropriately. The AOD at 550 nm can be estimated from DNI and precipitable water vapor. First, the Linke turbidity T_L is calculated from DNI for each time stamp using the formulation from Ineichen and Perez (2002). T_L is then used together with the precipitable water vapor and pressure to estimate the current AOD at 550 nm using the relation from Ineichen (2008). It is important that the DNI used to derive the AOD is not affected by clouds. It is therefore crucial to identify the sunny periods, for which no cloud is masking the sun. The algorithm to detect the clouds uses the T_L time series for all time stamps and its temporal gradient. In a first step a cloud is detected if $T_L > 13$ or if T_L varies strongly over time, i.e. if the absolute amount of the gradient between two time stamps is above 1.2/hour. The DNI is then compared to the clear sky DNI, which is derived from the lowest T_L in the examined time series. If the DNI for a time stamp is at least x % lower than the clear sky DNI, the time stamp is interpreted as cloudy. x is a variable threshold that depends on the air mass. Time stamps at solar noon with deviation larger than 10 % are classified as cloudy, however, time stamps at sun rise have to reach a deviation of 30 % (Hanrieder et al., 2016; Wilbert et al., 2016). For this calculation of the AOD, only the measured DNI from the RSI is available. This DNI is not yet corrected because an accurate estimation of the spectrum is needed for the spectral temperature correction, which already requires a good estimation of the AOD. In order to solve this problem, an iteration process is used, which is described in the following.

Before the cloud detection and the iteration process, a spectral temperature correction is done with the most basic assumptions about the spectrum. This is necessary, in order to detect clouds and start the iteration process from a better initial estimation. This preliminary correction is done with an estimation of the GHI, DHI and DNI spectra using an air mass of 1.5 and a default turbidity that can be specified for the site of interest. With these spec-

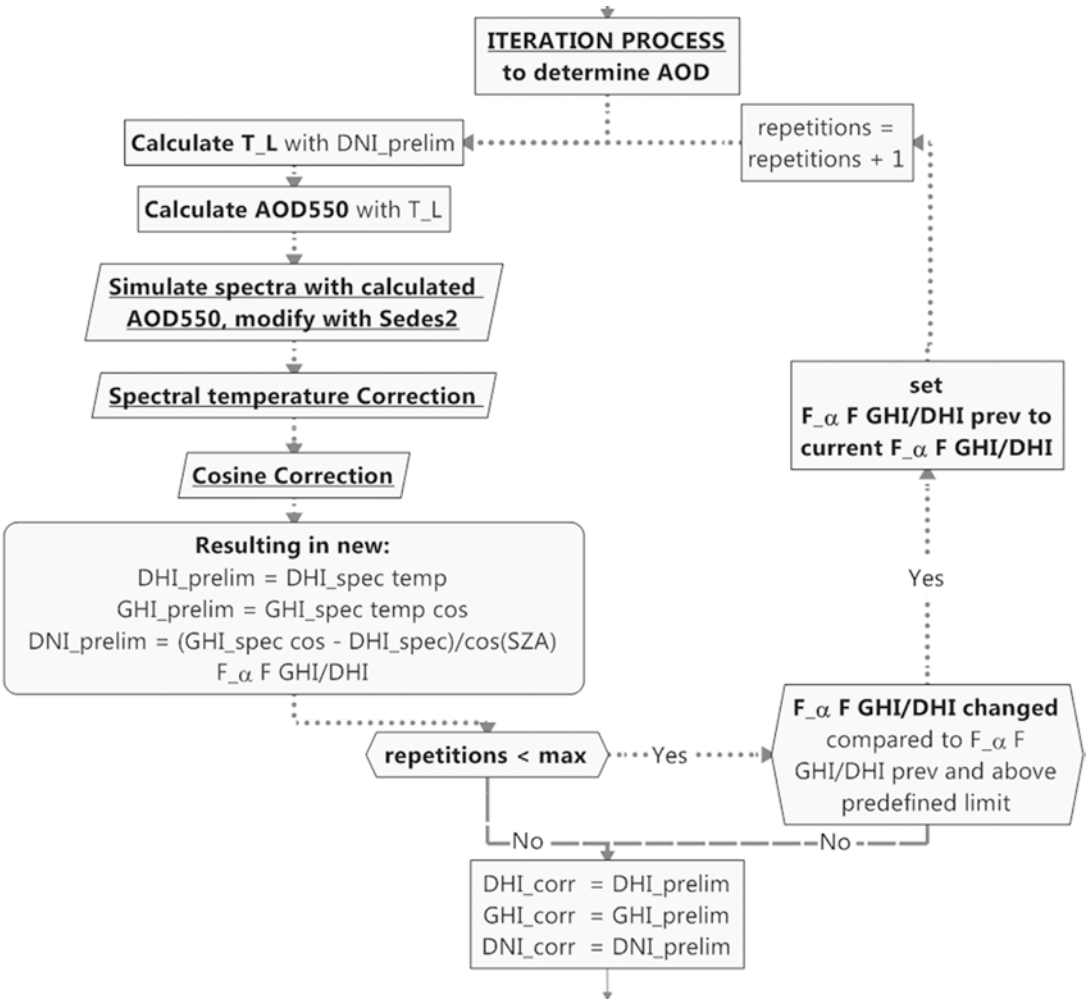

Figure 6: Iteration process of the correction method for the most accurate estimation of the AOD with the available DNI measurement of the RSI.

tra, a preliminary spectral temperature correction and cosine correction is performed on the entire GHI and DHI time series, which are already multiplied with the calibration factors g and d. These corrections result in the preliminary measurements GHI_{prelim} and DHI_{prelim} from which the DNI_{prelim} is calculated.

To identify the sunny time periods, when the sun is not masked by clouds, the cloud detection is used as explained in the paragraphs above. For each of the thus obtained sunny time stamps, the iteration process, displayed in Fig. 6, is started with GHI_{prelim}, DHI_{prelim} and DNI_{prelim}. First, the Linke turbidity is calculated using DNI_{prelim}. Then, the AOD at 550 nm is calculated. With this AOD at 550 nm and all other input parameters mentioned in the second paragraph of this section, the spectra of GHI, DHI and DNI are simulated with SMARTS 2.9.5 and cloud modified with the enhanced Sedes2 model. The cloud modification is necessary because clouds can still be present in the sky even if they do not mask the sun and affect the GHI and DHI spectra. With the modified spectra of the GHI and DHI, the specific spectral temperature correction factors for GHI and DHI, $F_{\alpha F,I}$, are calculated (see Section 2.1.2). The GHI and DHI, already multiplied with their respective calibration factors, are then spectral temperature corrected and the GHI is cosine corrected as described in Section 2.1.3. This results in DHI_{spectemp} and $GHI_{\text{spectempcos}}$, which define a new set of preliminary measurements for the examined sunny time stamp. From these two preliminary results, a new DNI_{prelim} is calculated.

If the spectral temperature correction factors $F_{\alpha F,I}$ for GHI and DHI deviate more than 0.0005 from the previous correction factors and are above a predefined limit of 1.1, the iteration is repeated until a maximum of 5 repetitions is reached. For the corrections that were performed for this paper, the mentioned break conditions were rarely met. If any of the break conditions are met, the next sunny time period is processed until AOD estimations for all sunny time periods are calculated.

Finally, all time periods for which the sun is masked are corrected using the temporally closest estimated AOD as an input parameter for the SMARTS and Sedes2 model. If the time difference between the current time period and the temporally closest estimated AOD is

Table 1: Station information of the three locations that are used in this paper. The climates are determined using Kottek et al. (2006), The Aeronet stations can be found via https://aeronet.gsfc.nasa.gov/cgi-bin/draw_map_display_aod_v3 and the direct links provided in the text.

Site	Location	Coordinates	Climate	Reference broad band radiometers	Aeronet station
CIEMAT's Plataforma Solar de Almería (PSA) Used for RSI calibration	Tabernas, Spain	37.091° N, 2.358° W, 500 m a.m.s.l.	arid, steppe, cold arid climate (BSk)	Kipp&Zonen pyrheliometer (CHP1), on automated solar tracker Kipp&Zonen pyranometers (CMP21)	Tabernas_PSA-DLR
NETRA's station	Greater Noida, New Delhi, India	28.502° N, 77.465° E, 195 m a.m.s.l.	warm temperature, dry winter, hot summer (Cwa)	Kipp&Zonen pyrheliometer (CHP1), on automated solar tracker Kipp&Zonen pyranometers (CMP21)	Gual_Pahari and New_Delhi
Lon station	Londrina, Paraná, Brazil	Exact location confidential, rough location see text	warm temperature, fully humid, warm summer (Cfb)	Kipp&Zonen pyrheliometer (CHP1), on automated solar tracker Kipp&Zonen pyranometers (CMP10)	Campo_Grande_SONDA

greater than three days a monthly average of the AOD is used. With this input, the physical correction is made following the basic principle described in Section 2.1 and Fig. 2 using the same functional dependences as used during the calibration. This results in the spectral temperature and cosine corrected GHI, the spectral temperature corrected DHI and the corresponding DNI as final corrected measurements. These corrections have to be made for each sensor and time range when it is deployed at a measurement site. For each new measurement site, the input parameters such as aerosol properties have to be adjusted once beforehand, but the calibration constants that were determined at one calibration site can be used without adapting.

3 Experimental set-up and evaluation of the method performance

Within this section the experimental set-up including the calibration sensors used in the experiment and field measurements is explained. The performance of the correction and calibration methods at different locations is illustrated and discussed. Finally, an analysis of options to improve the method is conducted. In order to quantify the correction results, two RSIs were calibrated at one location using the three calibration methods for *Geu*, *Vig* and the new physical correction functions. The RSIs were then deployed at two different locations in different climates than the calibration station. The measurements are then corrected with the three correction functions, all of which are not adjusted specifically to the new locations, and their performance is compared in terms of irradiance. Also intermediate results obtained during the correction process are evaluated using Aeronet data as a reference.

3.1 Measurement sites, used sensors and datasets

In this paper, the following three locations are used as displayed in Table 1.

A general description of CIEMAT's Plataforma Solar de Almería (PSA) in Tabernas, Spain can be found in Wilbert et al. (2013) and Pozo-Vázquez et al. (2011). The "cold" climate might be misleading as the average temperature is about 17 °C which is close to the common threshold to "hot arid climate" of 18 °C and as the average temperatures of the coldest month are about 7 to 10 °C and hence well above corresponding alternative thresholds of 0 °C and −3 °C. An Aeronet station near the reference and calibration station provides level 2.0 data, that is fully cloud and quality filtered, on atmospheric parameters for most of the period of interest (https://aeronet.gsfc.nasa.gov/cgi-bin/type_one_station_opera_v2_new?site=Tabernas_PSA-DLR&nachal=2&level=2&place_code=10). For one of the examined sensors (RSI-PY87333-1) one year of reference and RSI data from January 2015 to February 2016 are available from this site. The Aeronet station provides data for the entire time range except for February 2015, where it was offline. This sensor was then deployed at NETRA, India (see below). For the other examined sensor (RSI-PY88668-1), four months of reference and RSI data from April to August 2016 are available. But the Aeronet station was only online from June to August 2016, which is why the calibration data set is reduced to that time period. This RSI sensor was then deployed in Londrina, Brazil (see below).

The nearest Aeronet station to NETRA's station in Greater Noida, New Delhi, India that measured in the desired time range is located in Gual Pahari (28.426° N, 77.150° E, 250 m a.m.s.l.) which is about

Table 2: Used data for each evaluation step.

Evaluation step	RSI raw irradiance and sensor temp.	Rel. hum. ambient temp.	Reference irradiance measurement	Aeronet data as climatology	Aeronet data as time series
calibration	X		X		X
RSI corrected data measurement,	X	X		X	
evaluation of RSI irradiance data,	X	X	X	X	
evaluation of intermediate results involved in the correction process	X	X			X

32 km away from the station and provides 1.5 level Aeronet data (https://aeronet.gsfc.nasa.gov/cgi-bin/type_one_station_opera_v2_new?site=Gual_Pahari&nachal=0&year=16&aero_water=0&level=2&if_day=0&if_err=0&place_code=10&year_or_month=1). For the estimation of the Angström parameters, symmetry and asymmetry factor, level 2.0 Aeronet data from 2009 from the site in New Delhi (28.630° N, 77.175° E, 240 m a.m.s.l.) that is also about 32 km away from NETRA's station are used (https://aeronet.gsfc.nasa.gov/cgi-bin/type_one_station_opera_v2_new?site=New_Delhi&nachal=2&level=3&place_code=10). This choice is made because this station is located in the main wind direction from NETRA. That way, we assume that a better estimation of the aerosol type at NETRA can be made.

The Lon station in Londrina, Paraná, Brazil does not measure the current site pressure which is therefore estimated using the monthly average data from www.worldweatheronline.com/londrina-weather-averages/, that is measured at the Londrina airport, about 2.5 km away from the station. The nearest Aeronet stations are about 470 km away and located in Campo Grande, Sonda and Sao Paulo. Campo Grande, Sonda (20.438° S, 54.538° W, 677 m a.m.s.l.) provides 1.5 level Aeronet data for this evaluation (https://aeronet.gsfc.nasa.gov/cgi-bin/type_one_station_opera_v2_new?site=Campo_Grande_SONDA&nachal=0&year=25&aero_water=0&if_day=0&year_or_month=1&level=2&place_code=10). Even though the climate at the site is equatorial with a dry winter (Aw) (Kottek et al., 2006) the site is still chosen as source of Aeronet data for simplicity. At least the population of the cities is about the same, both cities are not near the coast and at about the same altitude at different sides of the Rio Paraná.

Based on Vuilleumier et al. (2014) we estimate the uncertainty for the 1 min thermopile radiometers as 1 %. Based on Holben et al. (1998) the uncertainty of the aerosol optical depth at 550 nm is estimated as +/−0.01 and that of the precipitable water vapor as 12 %.

The studied RSIs are Twin RSI manufactured by CSP Services equipped with LI- 200 sensor (Licor, 2004) for the irradiance measurements. For this work, one minute data resolution collected within 24 hours after a cleaning event is taken into consideration. This assures that the sensors are not affected by soiling. In addition, the automatic quality control described by Geuder et al. (2015) is used to discard suspicious data and only solar zenith angle below 85°, GHI and DHI measurements above 10 W/m^2 and DNI measurements above 300 W/m^2 are considered. All corrected RSI measurements that deviate more than 25 % from the reference measurement are assumed to be erroneous and are not used for the calculation of the calibration factors. The sensors at the NETRA station were cleaned following an irregular schedule, which means the available data set is reduced significantly and the time periods might be temporally far apart.

3.2 Evaluation method

To quantify the performance of the physical calibration and correction method, the two sensors are calibrated at the PSA and then deployed at Lon or NETRA. At both stations the RSI measurements are corrected with Geuder et al. (2008) (*Geu*), Vignola (2006) (*Vig*) and the physical correction method (*Phys*) to allow a benchmark. The calibration factors for the benchmark were derived at PSA. Note that the correction functions for *Geu* were derived at the PSA. The correction functions for *Vig* were derived at various sites in the USA. Evaluations are performed using several time periods at each site. Then, the mean bias and the root mean square deviation (RMSD) for GHI, DNI and DHI are calculated and compared as a measure for the performance of the calibration and correction methods. Later in Section 3.4 intermediate results of the correction method such as the aerosol optical depth are evaluated. The different involved data sets and their application are shown in Table 2.

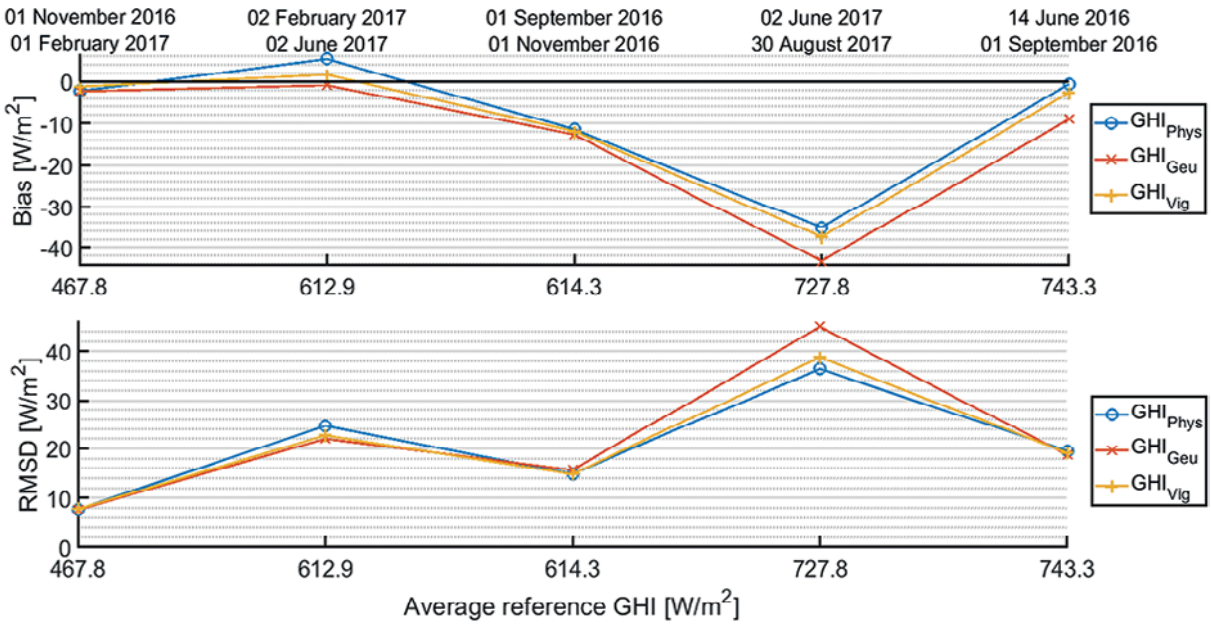

Figure 7: Mean bias and RMSD of corrected measurements from NETRA with calibration factors from the PSA for the GHI.

3.3 Performance with the calibration factors from the PSA at two locations

3.3.1 Correction results in NETRA, India

Fig. 7 displays the mean bias and RMSD of the corrected GHI measurements for five different time ranges. The different time ranges are displayed above each subplot. The x axis references the average GHI, measured with the thermopile pyranometer, for each time range.

Overall, the three correction methods perform similarly. The physical correction method is able to reduce the bias of the GHI measurements compared to *Geu* and *Vig* for three out of five periods. The highest RMSD of 36 W/m^2 occurs between June 2nd and August 30th, during which much of the weather was affected by the summer monsoon in New Delhi (Wang and Ho, 2001) and the application of the physical correction method yields a lower RMSD compared to the pre-existing methods in that time range. The summer monsoon time implies a challenge for the physical calibration method because the last calculated AOD from a sunny time stamp might be days or even weeks earlier. Especially the high bias of −35 W/m^2 in that time range could indicate that the Sedes2 model does not reach a sufficient accuracy for these weather conditions. However, the Phys method still outperformed the other correction methods for this time interval. Additionally, none of the correction methods show a seasonal deviation.

Fig. 8 displays the bias and RMSD of the corrected measurements after applying the different correction methods for the DNI in the same manner as for the GHI. The reference DNI that is displayed on the horizontal axis is measured with the pyrheliometer at NETRA for the specific correction time range.

Fig. 8 shows that the physical correction is able to reduce the bias of the corrected DNI measurements compared to *Geu* for all but one time period and compared to *Vig* for all but two time ranges. This is again remarkable because it shows that the systematic errors of the RSI measurement could be reduced more than with pre-existing methods. The RMSD for the DNI is reduced for all but one time range. For that time range the RMSD is increased by 3 W/m^2 in comparison to *Vig* and 5 W/m^2 compared to *Geu*. One possible explanation could be that the Angström exponents, which are estimated with Aeronet data from a selected year in New Delhi, might not fit the actually represent the aerosol type in that time period, yielding a higher bias and RMSD. It is worth mentioning that the uncertainty of the reference measurements is between 3 to 4 W/m^2.

This analysis of the measurement errors shows that the physical correction function is able to reduce the bias of the GHI and DNI measurements for three out of five time periods for NETRA's station. This shows that, the physical correction function is able to model the measurement characteristics of the RSI. A possible reason why the RMSD is not even more reduced for the GHI and DNI might be a wrong estimation of the input parameters describing the aerosols like the AOD and the Angström exponents and the application of the Sedes2 model that might not fit the cloud effects on the spectra well enough. This is further investigated in Section 3.4. Another reason for errors found could be deviations of the spectral response of each individual pyranometer compared to the assumed spectral response. This could be reduced in the future by measuring and using the individual spectral response of each sensor in the correction method. However, this would lead to higher sensor costs and the gained improvement was not tested. Since 1 min data was used for this evaluation, the RMSD is

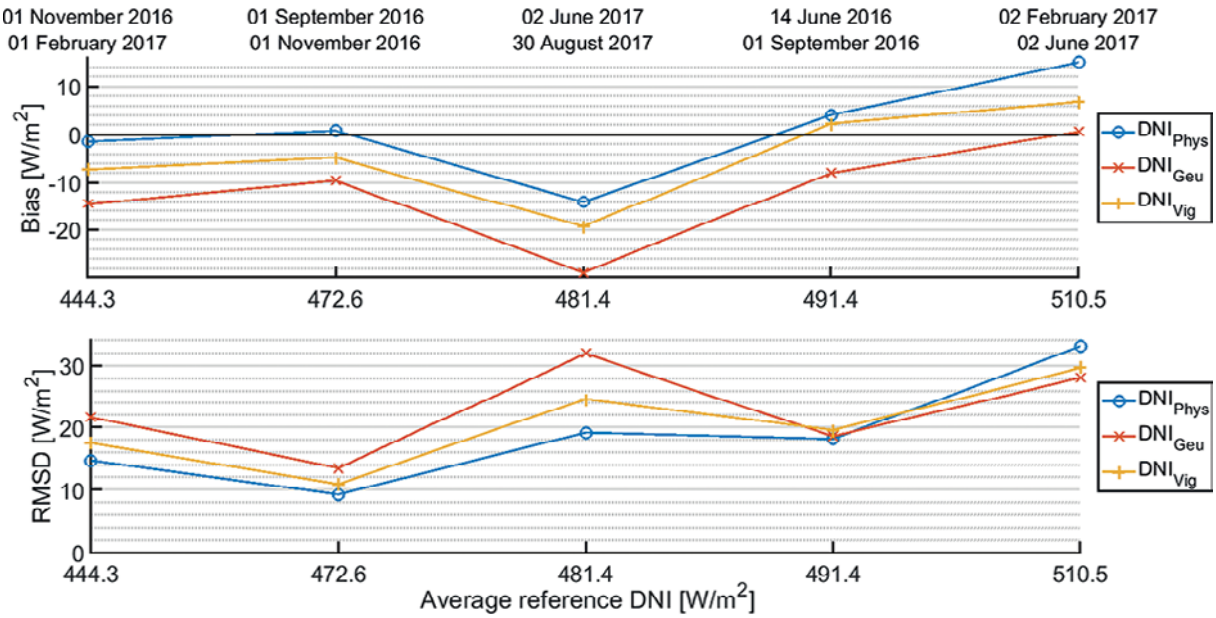

Figure 8: Mean bias and RMSD of corrected measurements from NETRA with calibration factors from the PSA for the DNI.

increased due to natural deviations of the measured irradiance values from the sensor. This is a source for the overall increased RMSD. Compared to the typical uncertainty of the *Vig*-corrected RSI data of about 2 % for GHI and 3 % for DNI (Wilbert et al., 2016) the deviations between the three methods are small in several of the investigated cases. However, cases for which the DNI and GHI bias and RMSD of the empirical methods are exceptionally high (~ 5–6 % RMSD, e.g. Netra GHI and DNI June–August 2017) are improved by the physical correction method. Also, it is worth pointing out that the good correction results of the physical correction method are achieved already with quite rudimentary estimations of the atmospheric conditions and aerosol type. It is also worth stressing that the estimation of the aerosol properties, α_1, α_2, single scattering albedo and asymmetry factor, stem from an evaluation of 2009 in New Delhi, which is about 27 km away from NETRA's site and a major aerosol source. It is expected that the measurement errors after the physical correction could be further reduced with an improvement of the aerosol input parameters and the Sedes2 model. The results suggest that the location dependence of the correction with calibration factors from the different climate at the PSA is reduced with the new methods.

3.3.2 Correction results in Londrina, Brazil

The calibration factors from a calibration time of one and a half months, from 17 July to 30 August 2016 at the PSA are tested using the three different correction methods at the Lon station in Londrina, Brazil. Three time ranges are examined and selected so that there is approximately the same number of data points in each interval. Since the station is located in the southern hemisphere, the time range includes spring, summer and fall at the site. Fig. 9 and 10 display the bias and RMSD of the corrected measurements for GHI and DNI respectively after the different correction methods are applied.

The results are shown in the same way as the NETRA correction results. For one time range the bias of the GHI is reduced compared to *Geu* and increased in comparison to *Vig*. For the other two time ranges the bias for the GHI measurement is increased by 1 to 3 W/m^2 with the physical method in comparison with *Vig* and 2 to 7 W/m^2 compared to *Geu*. Overall, the bias of all methods is small (<1.5 %). No improvement of the RMSD is achieved with the physical method and the results of all three correction methods are close to each other except for one time range. In that time range (18 November 2017 to 05 January 2018) cloudy situations prevailed, which might be an indication that the Sedes2 model is not applicable at the Londrina station.

For the DNI bias, the application of the physical correction method yields nearly the same result as the application of the pre-existing correction methods as Fig. 10 shows for two time ranges. In the time range of 18 November 2017 to 05 January 2018 the bias is increased to about 1.6 % with respect to the average reference DNI. The RMSD is decreased with the physical correction method for the other two time ranges to about 3.6 %.

There are a few possible explanations for the lack of improvement by the physical correction method in Londrina. No atmospheric pressure measurement is done in Londrina on ground level. The pressure is therefore estimated with monthly average values, which adds an uncertainty to the correction method and could lead to a bias in the correction results. The pressure is used to calculate the precipitable water vapor. The precipitable

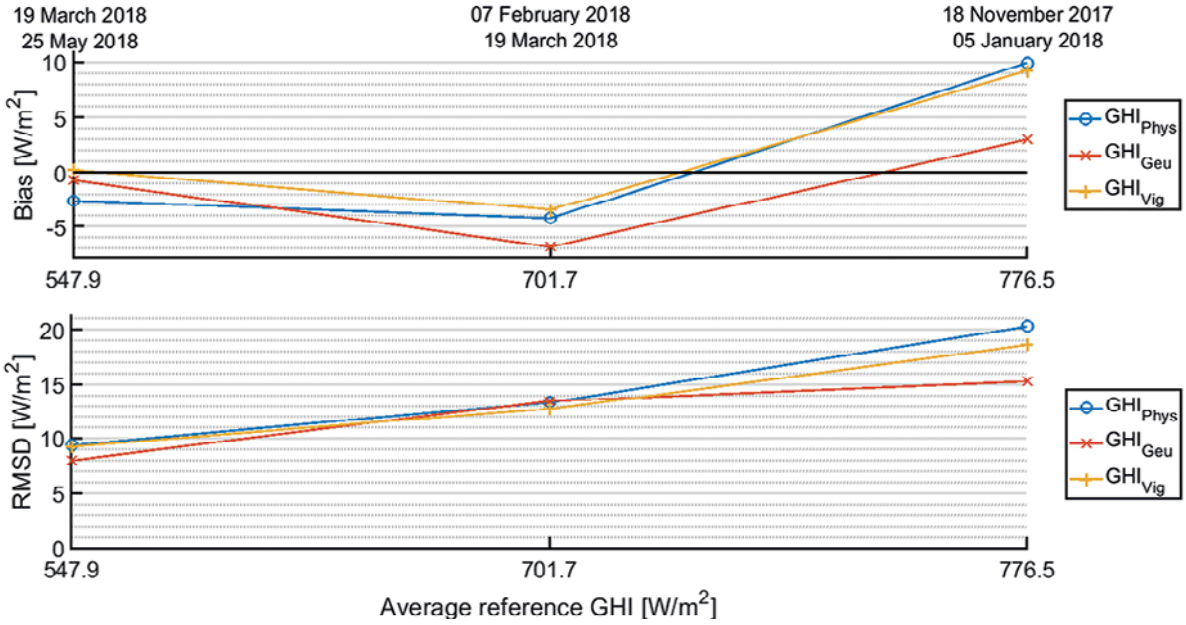

Figure 9: Mean bias and RMSD of corrected measurements from Londrina with calibration factors from the PSA for the GHI.

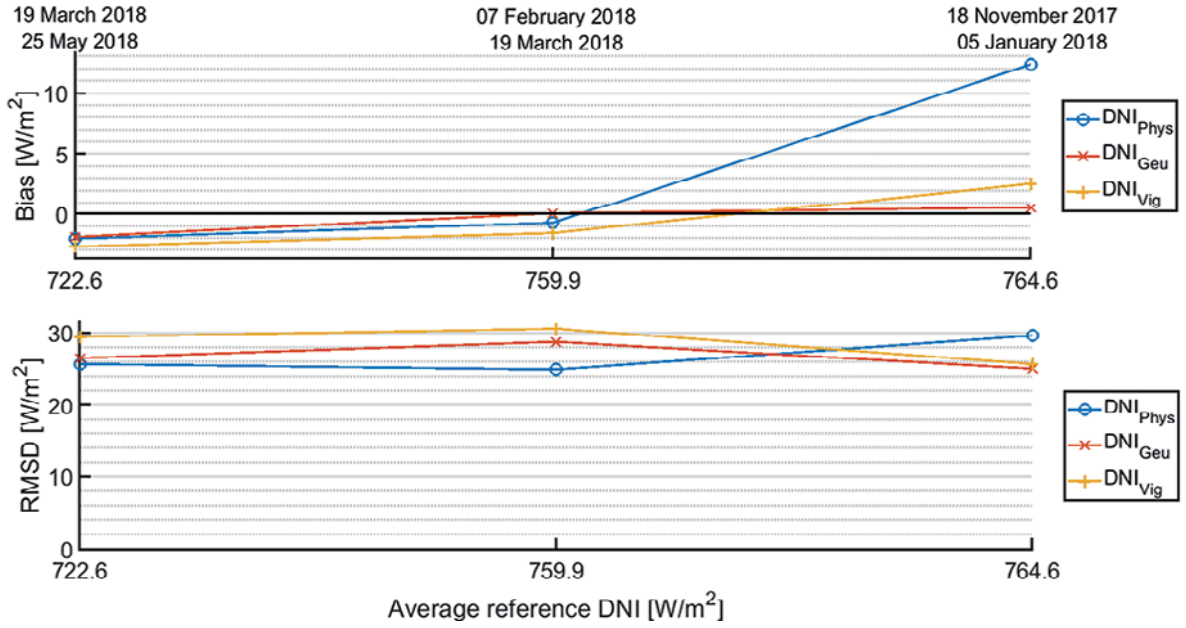

Figure 10: Mean bias and RMSD of corrected measurements from Londrina with calibration factors from the PSA for the DNI.

water vapor and pressure is then used to estimate the AOD at 550 nm. This is a key factor when simulating the spectrum with SMARTS. If the AOD at 550 nm is erroneous, the spectrum and therefore the entire physical corrections are erroneous.

An overall improvement of the input parameters especially with regard to the estimation of the Angström exponents, single scattering albedo and asymmetry factor should also be done because they stem from an Aeronet station that is about 470 km away and in a different climate. Better correction results might even be achieved with estimations of the aerosol type from a station that is further away from Londrina but has a comparable climate and population size.

In addition, all time ranges, but especially the time range from 18 November 2017 to 05 January 2018, that are examined, are heavily impacted by clouds which means that the influence of Sedes2 on the physical correction is quite high even though Sedes2 might not be applicable in Londrina. Myers (2012) evaluated simulated spectra and spectral measurements for Miami in Florida and Boulder in Colorado and found high deviations between the computed spectra by Sedes2 and spectral measurements especially in the wavelength range where the here used LI-COR sensor is sensitive. This shows that the Sedes2 model might not be applicable. The errors and possible enhancements of the Sedes2 should be investigated.

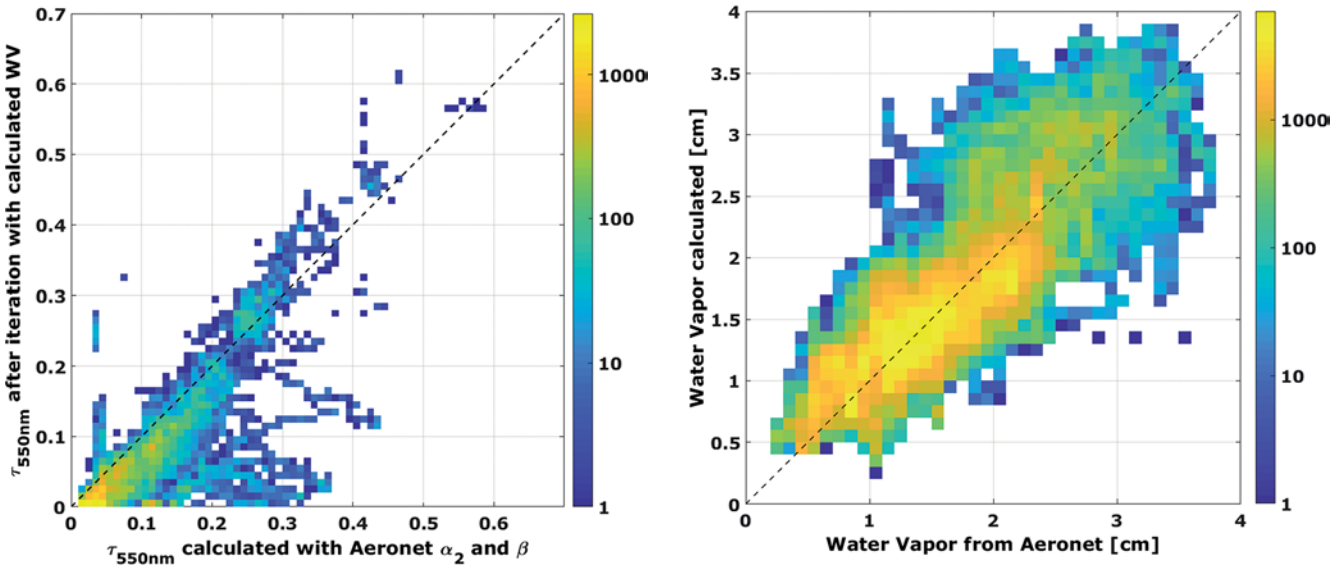

Figure 11: Evaluation of the AOD calculation by Ineichen (2008) and calculated precipitable water vapor by Garrison and Adler (1990) for the PSA, Spain. a) Calculated $\tau_{550\,\mathrm{nm}}$ after the iteration process in comparison with $\tau_{550\,\mathrm{nm}}$calculated from Aeronet data for one year and sunny time periods. b) Calculated precipitable water vapor compared to measured water vapor from Aeronet measurements for one year.

The possibly wrong input for the aerosol type could explain the increased bias that is observed for the GHI and DNI. Overall, there are uncertainties regarding the results in Londrina due to the quality of the input data. However, despite these uncertainties, the physical correction method is able to perform as well as the empirical correction methods Geu and Vig, which have been long term tested and are well-tried. The found deviations of the physical method and possible explanations are discussed in more detail in the next section.

3.4 Discussion and potential for improvement

Improvements in the accuracy of the aerosol data, the precipitable water vapor and the Sedes2 model can ultimately improve the physical correction method. Another reason for errors found could be deviations of the spectral response of each individual pyranometer compared to the assumed spectral response. This could be reduced in the future by measuring and using the individual spectral response of each sensor in the correction method. This section further evaluates the influence of the AOD and the precipitable water vapor. An improvement in finding default values for the Angström exponents, single scattering albedo and asymmetry factor could improve the method's performance significantly. The following sections investigate how well the iteration process of the physical correction estimates the AOD at 550 nm. The estimation of the AOD depends on the calculated precipitable water vapor. How well the calculation of the precipitable water vapor following Garrison and Adler (1990) fits the reference precipitable water vapor is also investigated. This analysis is done in the following two sections for PSA and NETRA.

3.4.1 AOD and precipitable water vapor estimation at PSA, Spain

The evaluation uses one year of data from PSA and the following approach to evaluate the accuracy of the AOD estimation. First, the AOD at 550 nm is estimated with the iteration process from the physical correction at the PSA over the course of one year for all sunny time stamps. The AOD at 550 nm is also calculated from the measurement of α_1 and β_2 from the Aeronet station as reference. The calculated precipitable water vapor is compared to the measurement with the Aeronet station as a reference. Version 2 Level 2 Aeronet data is used here. In Fig. 11 the results of the analysis are shown. On the y axis of Fig. 11a), the AOD at 550 nm after the iteration process is displayed. This AOD is estimated during the correction process with the calculated precipitable water vapor and is only calculated for sunny time stamps over the course of one year. On the x axis of Fig. 11a) the reference AOD is shown.

The comparison in Fig. 11a) shows that the AOD after the iteration deviates from the actual AOD in many cases. Fig. 11a) shows only data points that were categorized as sunny, which means that the algorithm did not detect a cloud in front of the sun. Few time periods were not categorized correctly and therefore show high $\tau_{550\,\mathrm{nm}}$ up to 0.3 after the iteration when the Aeronet station measured a rather low $\tau_{550\,\mathrm{nm}}$ of under 0.05 (vertical lines). There are a number of possible reasons why differences can be observed. In some case the Aeronet data points seem to be impaired by clouds since quite sudden AOD fluctuations are observed in the Aeronet time series. In such cases the Aeronet data shows AODs greater than the AOD estimated from the RSI data after the iteration. Another source for differences is that the function to obtain $\tau_{550\,\mathrm{nm}}$ from the T_L by Ineichen

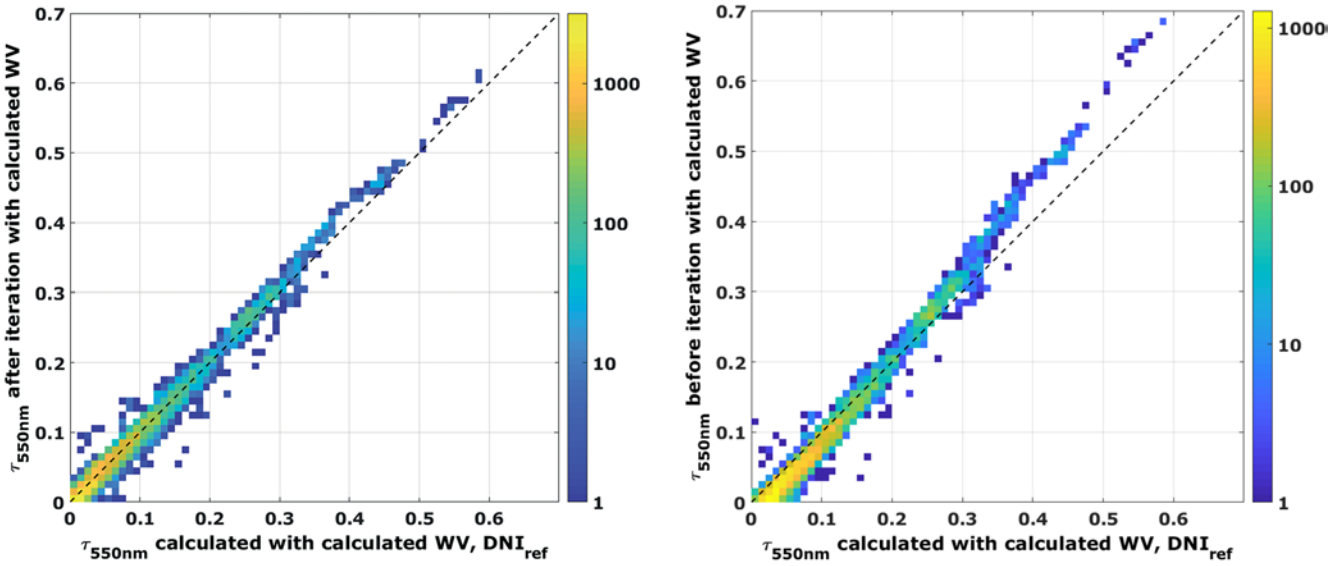

Figure 12: Evaluation of $\tau_{550\,nm}$ for sunny time stamps before and after the iteration at the PSA. a) Calculated $\tau_{550\,nm}$ after the iteration process in comparison with the $\tau_{550\,nm}$ calculated with calculated precipitable water vapor and the reference DNI. b) Calculated $\tau_{550\,nm}$ before the iteration process in comparison with the $\tau_{550\,nm}$ calculated with calculated water vapor and the reference DNI.

(2008) uses an urban aerosol type. This is a poor choice for the remote PSA that is located in a more rural environment and only about 40 km away from the coast. The aerosol type used in Ineichen (2008) is likely to correspond to an Angström exponent different from that measured at PSA by the sun photometer. Such an error of the Angström exponent translates to an error in $\tau_{550\,nm}$. Also, an error of the precipitable water vapor translates in an error of AOD. To determine the main source of the observed differences, further studies using Ineichen's method modified for the different aerosol type and DNI simulations with input of the Aeronet and from Ineichen (2008) should be made. Fig. 11b) shows the precipitable water vapor from the Aeronet station as the most accurate reference on the x axis and the calculated water vapor on the y axis. The color bar references how many measurement points fell into the corresponding pixels of the graphs. Fig. 11b) shows that the calculated precipitable water vapor is a good estimation of the present water vapor for most cases, although there is significant scatter.

It also needs to be investigated how the iteration process changes the estimated AOD for the sunny time stamps and which part of the deviations stem from the RSI's DNI measurement errors. When comparing the two obtained $\tau_{550\,nm}$ before and after the iteration to the calculated $\tau_{550\,nm}$ with the Linke turbidity obtained from the reference DNI and the calculated precipitable water vapor in Fig. 12, one notices that the iteration process is able to significantly improve the estimation of the AOD at 550 nm above 0.4.

3.4.2 AOD and precipitable water vapor estimation at NETRA, India

The same investigation as in the previous section is done for NETRA using Aeronet data from Gual Pahari. Note, that even though the investigation is done for one year as well, there are far less data points in Fig. 13a) then in Fig. 11a). The reason for that difference is that the investigation for NETRA only includes sunny time stamps with clean reference sensors.

Fig. 13a) shows the comparison between the $\tau_{550\,nm}$ obtained from the iteration process and the calculated $\tau_{550\,nm}$ from the Aeronet β_2 and α_2 at Gual Pahari. The $\tau_{550\,nm}$ after the iteration shows a significant bias of about 0.14. Additionally, the deviations between the reference AOD obtained with Aeronet and the AOD after the iteration are as high as 0.7 as opposed to a maximum deviation of 0.4 at PSA. In addition to the reasons for the deviations discussed for PSA, the spreading of the AOD values for NETRA can also stem from the different locations of the stations. The Aeronet station is situated about 50 meters higher than the NETRA station and about 32 km south-west. The main wind direction measured at the NETRA station is coming from New Delhi. The aerosols in the atmosphere above NETRA might therefore be different than the aerosols present at Gual Pahari.

The comparison in Fig. 13b) of the calculated precipitable water vapor from ambient temperature, relative humidity and pressure and the precipitable water vapor as measured at the Aeronet site shows that the water vapor is clearly underestimated for high water vapor contents above 4 cm. Again, one reason could be the distance between the NETRA and Gual Pahari stations. Another possible explanation could be that the approximation itself underestimates the precipitable water vapor for high water vapor contents.

3.4.3 Summary of the options to improve the physical methods

Overall, this investigation shows that there is room for improvement for the correction method. It could be in-

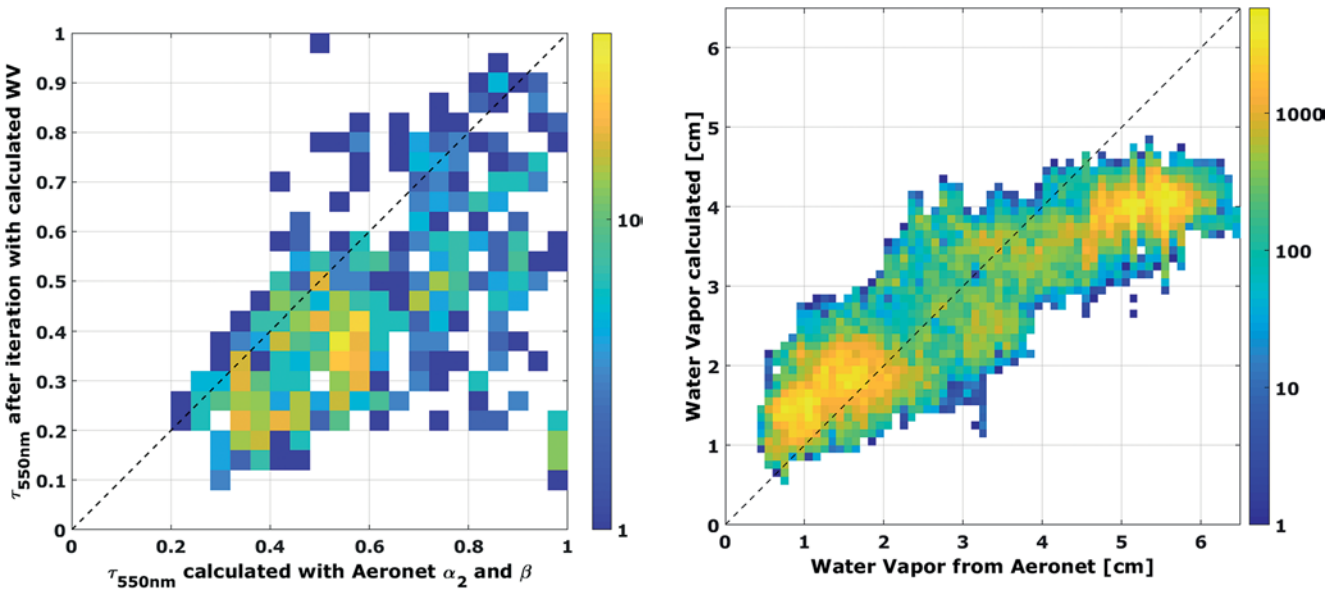

Figure 13: Evaluation of the AOD calculated by Ineichen (2008) and calculated precipitable water vapor by Garrison and Adler (1990) for NETRA. a) Calculated $\tau_{550\,nm}$ after the iteration process with $\tau_{550\,nm}$ calculated from Aeronet data from Gual Pahari. b) Calculated precipitable water vapor at NETRA compared to precipitable measured water vapor at Gual Pahari.

vestigated if it is possible to directly estimate β better from atmospheric parameters or if better results are achieved with a default aerosol type. The calculation of the precipitable water vapor by Garrison and Adler (1990) might also need improvement in particular in humid climates as the evaluation in NETRA showed. With such further enhancements the physical correction method might yield better results in terms of DNI and GHI deviations.

4 Conclusion and outlook

A new calibration and correction method for RSIs based on physical principals has been developed. For the first time, a combined spectral temperature correction is used for RSIs. The spectral temperature correction can reproduce the broadband corrections derived by King and Myers (1997) and Geuder et al. (2008). Differences between the so far used broadband temperature corrections can be explained and reproduced using the different spectra that might have been present during the experimental determination of the broadband temperature corrections. For the present study we used directional response measurements of the LI-200 and the newly found cosine correction function can be applied to the direct horizontal irradiance as opposed to the current correction sets where the empirical correction functions for the cosine and spectral effects of the calibration factors are interconnected and applied to the GHI. The calibration constants of each sensor and the presented correction functions can be applied at different measurement sites without adjustments.

The physical correction method shows satisfying results in regards of reducing the location dependence, especially in the previously problematic case of the NETRA station. The presented results demonstrate that a set of calibration and correction functions can be applied under different climate conditions. The physical correction method works well by removing the bias from the measurements of GHI and DNI and can reduce the RMSD most of the time, especially for the DNI component compared to the pre-existing method from Geuder et al. (2008). In comparison with the method of Vignola et al. (2017), the physical correction method yields a smaller bias for three and a smaller RMSD for four out of five time periods for the GHI and DNI measurements. In cases for which the empirical methods yielded exceptionally high RMSDs of about 5–6 % the physical correction method could reduce the RMSD. The correction results of the new method from Londrina, Brazil are analogous to those with the pre-existing methods from Geuder et al. (2008) and Vignola et al. (2017).

The iteration process of the correction method estimates an AOD that deviates noticeably from the Aeronet measurements. The AOD estimation from the iteration process and the RSI is close to the AOD calculated using Ineichen's equation and the pyrheliometer measurement. Hence, the reason for the deviation is not the RSI data itself, but the estimation method. Possible reasons include that the spectral variation of the AOD is not known and inappropriate Angström exponents might be used. Better estimations of the Angström exponents and their application are expected to improve the RSI corrections. The deviations can also be a result of possible errors of the Sedes2 model especially for the DNI and DHI spectral components. This should be further investigated especially at Londrina, Brazil. The AOD, the Angström exponents and the cloud effects could be better described using satellite or model derived datasets

such as the Copernicus Atmosphere Monitoring Service (CAMS) or the NASA Global Modeling and Assimilation Office. The application of such data sets is of great interest for further developments.

Another area for potential improvement is in the characterization of the photodiode pyranometers especially the spectral response of each individual sensor and the spectral temperature correction model. We aim to investigate this by using additional input from the PVSENSOR project. However, this option has to be evaluated carefully due to potentially too high costs.

A further advantage of the physical correction method is the possibility to derive more accurate uncertainty estimates compared to those for the empirical corrections. As the corrections are physical one can estimate the uncertainty of the used input parameters for each time stamp and propagate their errors to the final RSI measurement. This approach is more complex for the empirical correction functions as the uncertainty caused by the empirical steps can only be roughly estimated for an individual time stamp. Such an uncertainty analysis for the proposed method is an interesting topic for future work.

In conclusion, the new physical calibration and correction method reaches similar results compared to common empirical functions and shows no significant seasonal dependence. This is already achieved with rudimentary input parameters for the estimations of the GHI, DHI and DNI spectra. The results indicate that the physical approach reduces the problematic location dependence of the pre-existing calibration and correction methods. More stations at different locations should be examined to further investigate the results achieved by the physical correction. The physical correction and calibration method show promising results for a further improvement of the RSI accuracy. Better results could be achieved with an improvement of the spectral AOD, Angström exponent, single scattering albedo and precipitable water vapor calculation and cloud detection. Calculating the precipitable water vapor from the ambient temperature, pressure and relative humidity at the correction site induces a significant bias in humid climates and should therefore be possibly adjusted for these climate conditions. The cloud modification using the enhanced Sedes2 model is expected to bear a significant optimization potential.

Acknowledgments

We thank Fotovoltec, Solar Engineering for the supply of the measurements from Londrina. For establishing and maintaining the Aeronet sites at Campo Grande SONDA, Gual Pahari and New Delhi we thank E.B. Pereira, G. de Leeuw and P. Goloub and their respective staff. We thank ACTRIS and AERONET for their support with the stations including our own sun photometer at PSA. We thank Solar Consulting Services and C. Gueymard for providing the SMARTS software for this study.

Data availability

The used Aeronet data is available online through Aeronet. Data from PSA can be made available upon request. Data from Londrina and Greater Noida can be requested, but in this case third parties must be involved before possible distribution.

List of abbreviations

Abbreviation	Meaning
Aeronet	aerosol robotic network
α_i	Angström exponents
AOD	aerosol optical depth
β_i	Angström turbidity coefficient
Si	silicon
DHI	diffuse horizontal irradiance
DNI	direct normal irradiance
F_A	spectral response parameter or air mass correction (pre-existing)
F_B	cosine response parameter (pre-existing)
F_C	solar height or cat ear parameter
$F_{\cos}$	cosine correction factor (newly developed)
F_α	temperature correction factor (pre-existing)
$F_{\alpha F,I}$	spectral temperature correction factor (newly developed)
Geu	correction and calibration functions as described by Geuder et al. (2008)
GHI	global horizontal irradiance
$I_S(\lambda)$	spectral irradiance
λ	wavelength
C_{QE}	Constant to calculate the quantum efficiency from the spectral response
QE	quantum efficiency; The yield of electrons per photon.
RSI	Rotating Shadowband Irradiometer
RSMD	root mean square deviation
Sedes2	enhanced model for cloud modification of irradiance spectra by Nann and Riordan (1990); Nann and Riordan (1991); Myers (2012) altered according to Jessen et al. (2018)
SMARTS	A Simple Model of the Atmospheric Radiative Transfer of Sunshine; simulation software for solar spectra on the earth's surface by Gueymard (1995, 2005)
$R_{bb}(\lambda)$	responsivity of the pyranometer to broadband irradiance
$R_S(\lambda)$	spectral response as a function of wavelength
SZA	solar zenith angle
T_L	Linke turbidity
τ_λ	AOD at wavelength λ
Vig	correction and calibration functions described by King and Myers (1997); Augustyn et al. (2004); Vignola (2006)
WV	precipitable water vapor

References

ASTM, 2012: G173-03, Standard Tables for Reference Solar Spectral Irradiances. Direct Normal and Hemispherical on 37° Tilted Surface. – ASTM, ASTM International, DOI:10.1520/G0173-03R12.

ASTM, 2016: G214-15, Standard Test Method for Intergration of Digital Spectral Data for Weathering and Durability Applications. – ASTM, ASTM International. **G214–15**, DOI:10.1520/G0214-15.

Augustyn, J., T. Geer, T. Stoffel, F. Vignola, R. Kessler, E. Kern, R. Little, B. Boyson, 2004: Update of Algorithm to Correct Direct Normal Irradiance Measurements Made with a Rotating Shadow Band Pyranometer. – Solar 2004 Conference. Portland, OR, American Solar Energy Soc., 295–302.

Batlles, F., F. Olmo, L. Alados-Arboledas, 1995: On shadowband correction methods for diffuse irradiance measurements. – Solar Energy **54**, 105–114.

Driesse, A. , 2018: PV – Performance Labs internal report.

Driesse, A., W. Zaaiman, D. Riley, N. Taylor, J. Stein, 2015: Indoor and Outdoor Evaluation of Global Irradiance Sensors. – 31st European Photovoltaic Solar Energy Conference, 14–18 September 2015, Hamburg, Germany.

Garrison, J.D., G.P. Adler, 1990: Estimation of precipitable water over the United States for application to the division of solar radiation into its direct and diffuse components. – Solar Energy **44**, 4: 225–241, DOI:10.1016/0038-092X(90)90151-2.

Geuder, N., V. Quaschning, 2006. Soiling of irradiation sensors and methods for soiling correction. – Solar Energy **80**, 1402–1409.

Geuder, N., B. Pulvermüller, O. Vorbrugg, 2008: Corrections for rotating shadowband pyranometers for solar resource assessment. – Solar Energy + Applications. San Diego, USA, Proceedings of SPIE 70460, International Society for Optical Engineering, Society of Photo-Optical Instrumentation Engineers, DOI:10.1117/12.797472.

Geuder, N., M. Hanussek, J. Haller, R. Affolter, S. Wilbert, 2011: Comparison of Corrections and Calibration Procedures for Rotating Shadowband Irradiance Sensors. SolarPACES Conference, Granada, Spain.

Geuder, N., F. Wolfertstetter, S. Wilbert, D. Schüler, R. Affolter, B. Kraas, E. Lüpfert, B. Espinar, 2015: Screening and Flagging of Solar Irradiation and Ancillary Meteorological Data. – Energy Procedia **69**, 1989–1998, DOI:10.1016/j.egypro.2015.03.205.

Geuder, N., R. Affolter, O. Goebel, B. Dahleh, M. Al Khawaja, S. Wilbert, B. Pape, B. Pulvermüller, 2016: Validation of Direct Beam Irradiance Measurements From Rotating Shadowband Irradiometers in a Region With Different Atmospheric Conditions. – J. Solar Energy Engin. **138**, 051007–051007, DOI:10.1115/1.4034070.

Gueymard, C., 1995: SMARTS2, a simple model of the atmospheric radiative transfer of sunshine: algorithms and performance assessment. – Rep. FSEC-PF-270-95.

Gueymard, C., 2001: Parameterized transmittance model for direct beam and circumsolar spectral irradiance. – Solar Energy **71**, 5: 325–346, DOI:10.1016/S0038-092X(01)00054-8.

Gueymard, C.A., 2005: SMARTS code, version 2.9.5. – USER'S MANUAL For Windows.

Hanrieder, N., M. Sengupta, Y. Xie, S. Wilbert, R. Pitz-Paal, 2016. Modeling beam attenuation in solar tower plants using common DNI measurements. – Solar Energy **129**, DOI:10.1016/j.solener.2016.01.051.

Hishikawa, Y., M. Yoshita, H. Ohshima, K. Yamagoe, H. Shimura, A. Sasaki, T. Ueda, 2018: Temperature dependence of the short circuit current and spectral responsivity of various kinds of crystalline silicon photovoltaic devices. – Japan. J. Appl. Phys. **57**, 08RG17, DOI:10.7567/JJAP.57.08RG17.

Holben, B., T. Eck, I. Slutsker, D. Tanre, J. Buis, A. Setzer, E. Vermote, J. Reagan, Y. Kaufman, T. Nakajima, 1998. AERONET – A federated instrument network and data archive for aerosol characterization. Remote Sensing of Environment **66**, 1–16, DOI:10.1016/S0034-4257(98)00031-5.

Ineichen, P. , 2008: Conversion function between the Linke turbidity and the atmospheric water vapor and aerosol content. – Solar Energy **82**, 1095–1097, DOI:10.1016/j.solener.2008.04.010.

Ineichen, P., R. Perez, 2002: A new airmass independent formulation for the Linke turbidity coefficient. – Solar Energy **73**, 151-157, DOI:10.1016/S0038-092X(02)00045-2.

Jessen, W., S. Wilbert, B. Nouri, N. Geuder, H. Fritz, 2016: Calibration methods for rotating shadowband irradiometers and optimizing the calibration duration. – Atmos. Meas. Tech. **9**, 1601–1612, DOI:10.5194/amt-9-1601-2016.

Jessen, W., S. Wilbert, L. Zarzalejo Tirado, L. Ramirez Santigosa, R. Valenzuela Balderrama, J. Liria, B. Nouri, N. Hanrieder, 2017: Calibration Procedures for Rotating Shadowband Irradiometers. – SFERA II.

Jessen, W., S. Wilbert, C.A. Gueymard, J. Polo, Z. Bian, A. Driesse, A. Habte, A. Marzo, P.R. Armstrong, F. Vignola, L. Ramírez, 2018: Proposal and evaluation of subordinate standard solar irradiance spectra for applications in solar energy systems. – Solar Energy **168**: 30–43, DOI:10.1016/j.solener.2018.03.043.

Kasten, F., A.T. Young, 1989: Revised optical air mass tables and approximation formula. – Applied Optics **28**, 4735–4738, DOI:10.1364/AO.28.004735.

Kern, E.C. , 2010. Calibration Methods for Silicon Photodiode Pyranometers used in Rotating Shadowband Radiometers. – SolarPACES Conference, Perpignan, France.

King, D.L., D.R. Myers, 1997: Silicon-photodiode pyranometers: Operational characteristics, historical experiences, and new calibration procedures. – Photovoltaic Specialists Conference, IEEE, 1285–1288, DOI:10.1109/PVSC.1997.654323.

King, D.L., J.A. Kratochvil, W.E. Boyson, 1997: Measuring solar spectral and angle-of-incidence effects on photovoltaic modules and solar irradiance sensors. – Paper read at Conference Record of the Twenty Sixth IEEE Photovoltaic Specialists Conference-1997.

King-Smith, R.D., R.J. Needs, V. Heine, M.J. Hodgson, 1989: A First-Principle Calculation of the Temperature Dependence of the Indirect Band Gap of Silicon. – Europhysics Letters **10**, 569–574, DOI:10.1209/0295-5075/10/6/011.

Komhyr, W., R. Grass, R. Leonard, 1989: Dobson Spectrophotometer 83: a standard for total ozone measurements, 1962–1987. – J. Geophys. Res. **94**, 9847–9861, DOI:10.1029/JD094iD07p09847.

Kottek, M., J. Grieser, C. Beck, B. Rudolf, F. Rubel, 2006: World Map of the Köppen-Geiger climate classification updated. – Meteorol. Z. **15**, 259–263, DOI:10.1127/0941-2948/2006/0130.

Licor, 2004: Radiation measurement Instruments. – LI-COR Biosciences.

London, J., R. Bojkov, S. Oltmans, J. Kelley, 1976: Atlas of the Global Distribution of Total Ozone July 1957–June 1967. – NCAR Technical Note 1331STR, National Center for Atmospheric Research, Boulder, CO, 276 pp.

Maxwell, E.L., S.M. Wilcox, C. Cornwall, B. Marion, S.H. Alawaji, M. b. Mahfoodh, A. Al-Amoudi, 1999: Progress Report for Annex II – Assessment of Solar Radiation Resources in Saudi Arabia 1993–1997, NREL/TP-560-25374, National Renewable Energy Lab., Golden, CO (US).

Michalsky, J.J. , 1988: The Astronomical Almanac's algorithm for approximate solar position (1950–2050). – Solar Energy **40**, 227-235, DOI:10.1016/0038-092X(88)90045-X.

Myers, D.R. , 2012. Direct beam and hemispherical terrestrial solar spectral distributions derived from broadband hourly solar radiation data. – Solar Energy **86**, 2771–2782, DOI: 10.1016/j.solener.2012.06.014.

Nann, S., C. Riordan, 1990: Solar Spectral Irradiance Under Overcast Skies. – 21st IEEE Photovoltaic Specialists Conference. Orlando, IEEE, DOI:10.1109/PVSC.1990.111789.

Nann, S., C. Riordan, 1991. Solar spectral irradiance under clear and cloudy skies: Measurements and a semiempirical model. – J. Appl. Meteor. **30**, 447–462, DOI:10.1175/1520-0450(1991)030<0447:SSIUCA>2.0.CO;2.

Olsen, S.C., J.T. Randerson, 2004. Differences between surface and column atmospheric CO_2 and implications for carbon cycle research. – J. Geophys. Res. **109**, D02301, DOI:10.1029/2003JD003968.

Pape, B., J. Batlles, N. Geuder, R.Z. Piñero, F. Adan, B. Pulvermueller, 2009: Soiling Impact and Correction Formulas in Solar Measurements For CSP Projects. – SolarPaces, Berlin.

Pozo-Vázquez, D., S. Wilbert, C. Gueymard, L. Alados-Arboledas, F.J. Santos-Alamillos, M.J. Granados-Muñoz, 2011: Interannual Variability of Long Time Series of DNI and GHI at PSA, Spain. –SolarPACES Conference, Granada, Spain.

Rajkanan, K., R. Singh, J. Shewchun, 1979. Absorption coeffiecient of silicon for solar cell calculations. – Solid-State Electronics **22**, 793–795, DOI:10.1016/0038-1101(79)90128-X.

Sengupta, M., A. Habte, C. Gueymard, S. Wilbert, D. Renné, P. Blanc, A. Dobos, E. Lorenz, R. Meyer, D. Myers, L. Ramírez, K.P. Nielsen, A. Lopez, J. Kleissl, J. Remund, J.A. Ruiz-Arias, R. Perez, J. Polo, L.M. Pomares, M. Suri, T. Stoffel, F. Vignola, S. Wilcox, J. Wood, Y. Xie, L. Zarzalejo , 2017: Best Practices Handbook for the Collection and Use of Solar Resource Data for Solar Energy Applications. – Second Edition, ISBN: NREL/TP-5D00-68886.

Vignola, F. , 2006: Removing Systematic Errors from Rotating Shadowband Pyranometer Data. – Proceedings American Solar Energy Society.

Vignola, F., Z. Derocher, J. Peterson, L. Vuilleumier, C. Félix, J. Gröbner, N. Kouremeti, 2016: Effects of changing spectral radiation distribution on the performance of photodiode pyranometers. – Solar Energy **129**, 224–235, DOI: 10.1016/j.solener.2016.01.047.

Vignola, F., J. Peterson, S. Wilbert, P. Blanc, N. Geuder, C. Kern, 2017: New methodology for adjusting rotating shadowband irradiometer measurements. – AIP Conference Proceedings **1850**, 140021, DOI:10.1063/1.4984529.

Vignola, F., J. Peterson, F. Mavromatakis, S. Wilbert, A. Forstinger, M. Dooraghi, M. Sengupta, 2019: Removing biases from rotating shadowband radiometers. AIP Conference Proceedings 2126(1): 190017. DOI:10.1063/1.5117714.

Vuilleumier, L., M. Hauser, C. Félix, F. Vignola, P. Blanc, A. Kazantzidis, B. Calpini, 2014: Accuracy of ground surface broadband shortwave radiation monitoring. – J. Geophys. Res. Atmos., published online: https://hal-mines-paristech.archives-ouvertes.fr/hal-01112611/file/jgrd51847.pdf

Vuilleumier, L., C. Félix, F. Vignola, P. Blanc, J. Badosa, A. Kazantzidis, 2017: Performance evaluation of radiation sensors for the solar energy sector. – Meteorol. Z. **26**, 485–505, DOI:10.1127/metz/2017/0836.

Wang, B., L. Ho, 2001. Rainy season of the Asian-Pacific Summer Monsoon. – J. Climate **15**, 386–398, DOI:10.1175/1520-0442(2002)015<0386:RSOTAP>2.0.CO;2.

Wilbert, S. , 2014: Determination of Circumsolar Radiation and its Effect on Concentrating Solar Power. – Dr. rer. nat PhD thesis, Rheinisch-Westfälische Technische Hochschule Aachen, DLR, http://darwin.bth.rwth-aachen.de/opus3/volltexte/2014/5171/ (acessed 16.03.2019).

Wilbert, S., B. Reinhardt, J. DeVore, M. Röger, R. Pitz-Paal, C. Gueymard, R. Buras, 2013: Measurement of Solar Radiance Profiles With the Sun and Aureole Measurement System. – J. Solar Energy Engineer. **135**, 041002-041002, DOI:10.1115/1.4024244.

Wilbert, S., N. Geuder, M. Schwandt, B. Kraas, W. Jessen, D.R. Meyer, B. Nouri, 2015: Task 46: Best Practices for Solar Irradiance Measurements with Rotating Shadowband Irradiometers. IEA SHC Solar Update Newsletter. – IEA / SHC. **62**, 10–11, http://www.iea-shc.org/data/sites/1/publications/2015-11-Solar-Update-Newsletter.pdf (acessed 16.03.2019).

Wilbert, S., S. Kleindiek, B. Nouri, N. Geuder, A. Habte, M. Schwandt, F. Vignola, 2016: Uncertainty of rotating shadowband irradiometers and Si-pyranometers including the spectral irradiance error. – AIP Conference Proceedings 1734, 150009, DOI:10.1063/1.4949241.

Wilbert, S., M. Röger, J. Csambor, M. Breitbach, F. Klinger, B. Nouri, N. Hanrieder, F. Wolfertstetter, D. Schüler, S. Shaswattam, N. Goswami, S. Kumar, A. Ghennioui, R. Affolter, N. Geuder, B. Kraas, 2018: Sunshape measurements with conventional rotating shadowband irradiometers. – AIP Conference Proceedings **2033**, 190016, DOI:10.1063/1.5067201.

The pdf version (Adobe Java Script must be enabled) of this paper includes an electronic supplement:
Table of content – Electronic Supplementary Material (ESM)

Figure: Appendix 1